Fixed Point Analysis of Douglas–Rachford Splitting for Ptychography and Phase Retrieval*

Albert Fannjiang† and Zheqing Zhang‡

Abstract. Douglas–Rachford splitting (DRS) methods based on the proximal point algorithms for the Poisson and Gaussian log-likelihood functions are proposed for ptychography and phase retrieval. Fixed point analysis shows that the DRS iterated sequences are always bounded explicitly in terms of the step size and that the fixed points are attracting if and only if the fixed points are regular solutions. This alleviates two major drawbacks of the classical Douglas–Rachford algorithm: slow convergence when the feasibility problem is consistent and divergent behavior when the feasibility problem is inconsistent. Fixed point analysis also leads to a simple, explicit expression for the optimal step size in terms of the spectral gap of an underlying matrix. When applied to the challenging problem of *blind* ptychography, which seeks to recover both the object and the probe simultaneously, alternating minimization with the DRS inner loops, even with a far from optimal step size, converges geometrically under the nearly minimum conditions established in the uniqueness theory.

1. Introduction. Phase retrieval may be posed as an inverse problem in which an object vector with certain properties is to be reconstructed from the intensities of its Fourier transform. By encoding the properties and the Fourier intensities as constraint sets, phase retrieval can be cast as a feasibility problem, i.e., the problem of finding a point in the intersection of the constraint sets. The challenge is that the intensities of the Fourier transform result in a nonconvex constraint set (a high dimensional torus of variable radii).

Projection algorithms comprise a general class of iterative methods for solving feasibility problems by projecting onto each of the constraint sets at each step [1]. The most basic projection algorithm is von Neumann's alternating projections (AP) (a.k.a. error reduction in phase retrieval [23]). However, AP tends to stagnate when applied to phase retrieval, resulting in poor performance.

A better method than AP is the classical Douglas–Rachford algorithm (a.k.a. averaged alternating reflections (AAR)) [13, 25, 35, 25], which apparently can avoid the stagnation problem in many nonconvex problems. When applied to phase retrieval, the classical Douglas–Rachford algorithm is a special case of Fienup's hybrid-input-output algorithm [3, 23].

---

†Corresponding author. Department of Mathematics, UC Davis, Davis, CA 95616-8633 (fannjiang@math.ucdavis.edu).
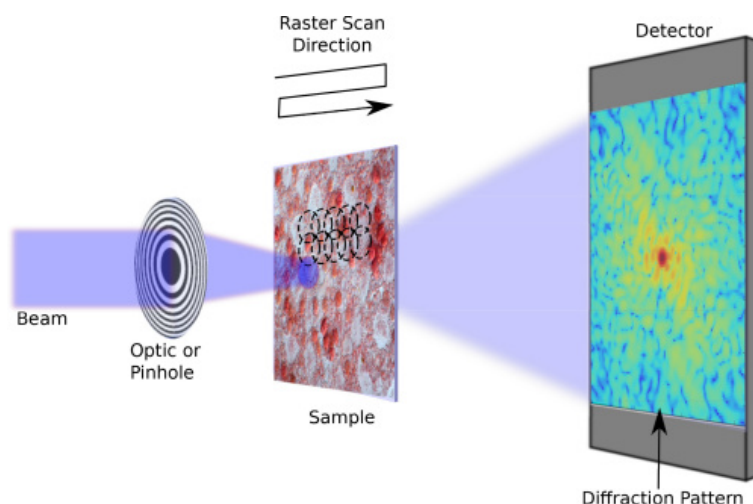‡Department of Mathematics, UC Davis, Davis, CA, 95616 (zheqing@math.ucdavis.edu).

Figure 1. *Simplified ptychographic set-up showing a Cartesian grid used for the overlapping raster scan positions* [43]. *See Appendix* A *for details.*

In addition to the standard phase retrieval, AAR has been applied to ptychography under the name of difference map [51, 50, 54]. Ptychography uses a localized coherent probe to illuminate different parts of an unknown extended object and collect multiple diffraction patterns as measurement data (Figure 1). The redundant information in the overlap between adjacent illuminated spots is then exploited to improve phase retrieval methods [47, 44]. Recently ptychography has been extended to the Fourier domain [57, 45]. In Fourier ptychography, illumination angles are scanned sequentially with a programmable array source with the diffraction pattern measured at each angle [53, 32]. Tilted illumination samples different regions of Fourier space, as in synthetic-aperture and structured-illumination imaging.

Local, linear convergence of AAR as applied to phase retrieval as well as ptychography was recently proved in [9, 10]. Conditions for global convergence, however, are not known. Numerical evidence points to a sublinear rate when convergence happens. On the other hand, for inconsistent feasibility problems, AAR iteration is known to diverge to infinity even in the convex case (see Proposition 2.1(ii)). This poses a great challenge to AAR when the data contain noise because in phase retrieval the dimension of the measurement data is much higher than that of the unknown object (an overdetermined system).

The purpose of this work is to develop reconstruction schemes based on more general Douglas–Rachford splitting (DRS) with adjustable step sizes, perform the fixed point analysis, and demonstrate numerical convergence. AAR is the limiting case of DRS.

The DRS method is an optimization method based on proximal operators, a natural extension of projections, and is closely related to the alternating direction method of multipliers (ADMM). The performance of DRS and ADMM in the nonconvex setting depends sensitively on the choice of the loss functions as well as the step sizes. Typically, global convergence of DRS requires a loss function possessing a uniformly Lipschitz gradient and sufficiently large step sizes [9, 33, 30], both of which, however, tend to hinder the performance of DRS.

In this paper, the loss functions are based on the log-likelihood function for the most important Poisson noise, which does not have a uniformly Lipschitz gradient, with an optimal step size, which is necessarily quite large.

We show by a fixed point analysis that the DRS method is well-behaved in the sense that the DRS iterated sequences are always bounded (explicitly in terms of the step size) and that the fixed points are attracting if and only if the fixed points are regular solutions. In other words, the DRS methods remove AAR's two major drawbacks: slow convergence when the feasibility problem is consistent and divergent behavior when the feasibility problem is inconsistent.

Moreover, the fixed point analysis leads to the determination of the optimal step size and, along with it, simple and efficient algorithms with no tuning parameter (averaged projection-reflection). The main application considered is the more challenging form of ptychography called *blind ptychography* which seeks to recover both the unknown object and the probe function simultaneously. When properly initialized, the DRS algorithms with the optimal step size converge globally and geometrically to the true solution modulo the inherent ambiguities.

The rest of the paper is organized as follows. In section 3, we introduce the DRS method as the key ingredient of our reconstruction algorithms, Gaussian-DRS and Poisson-DRS. We give the fixed point and stability analysis in sections 4, 5, and 6. In section 7, we discuss the selection of the optimal step size. In section 8, we discuss the application to blind ptychography, and in section 9, we present numerical experiments. In Appendix A, we discuss the structure of the measurement matrices. In Appendix B, we show that Gaussian-DRS is an asymptotic form of Poisson-DRS. In Appendix D we give a perturbation analysis for the Poisson DRS. In Appendix E, we analyze the eigenstructure of the measurement matrices. We conclude in section 10. A preliminary version of the present work is given in [20].

2. Averaged alternating reflections. The classical Douglas–Rachford algorithm is based on the following characterization of *convex* feasibility problems.

Let X and Y be the constraint sets. Let P_X be the projection onto X and $R_X = 2P_X - I$ the corresponding reflector. P_Y and R_Y are defined likewise. Then [26]

$$(2.1) \qquad u \in X \cap Y \quad \text{if and only if} \quad u = R_Y R_X u.$$

The latter fixed point equation motivates the Peaceman–Rachford (PR) method: For $k = 0, 1, 2, \dots$

$$u_{k+1} = R_Y R_X y_k.$$

The classical Douglas–Rachford algorithm is the *averaged* version of PR: For $k = 0, 1, 2, \dots$

$$(2.2) \qquad u_{k+1} = \frac{1}{2} u_k + \frac{1}{2} R_Y R_X u_k,$$

hence the name *averaged alternating reflections*.

A standard result for AAR in the convex case is this.

Proposition 2.1 (see [5]). *Suppose X and Y are closed and convex sets of a finite-dimensional vector space E. Let $\{u_k\}$ be an AAR-iterated sequence for any $u_1 \in E$. Then one of the following alternatives holds:*

(i) $X \cap Y \neq \emptyset$ and (u_k) converges to a point u such that $P_X u \in X \cap Y$;

(ii) $X \cap Y = \emptyset$ and $\|u_k\| \to \infty$.

In the consistent case (i), the limit point u is a fixed point of the AAR map (2.2), which after projection is in $X \cap Y$. However, the convergence rate of AAR is in general sublinear [29, 2]. The inconsistent case (ii) arises from noisy data or modeling errors resulting in divergent AAR iterated sequences, a major drawback of AAR since the inconsistent case is prevalent with noisy data because of the higher dimension of data compared to the object.

The AAR map (2.2) is often written in the form

$$(2.3) \qquad u_{k+1} = u_k + P_Y R_X u_k - P_X u_k,$$

which is equivalent to the three-step iteration

$$(2.4) \qquad y_k = P_X u_k;$$
$$(2.5) \qquad z_k = P_Y(2y_k - u_k) = P_Y R_X u_k,$$
$$(2.6) \qquad u_{k+1} = u_k + z_k - y_k.$$

2.1. Phase retrieval as feasibility. For any finite-dimensional vector u, define its modulus vector $|u|$ as $|u|[j] = |u[j]|$ and its phase vector $\mathrm{sgn}(u)$ as

$$\mathrm{sgn}(u)[j] = \begin{cases} 1 & \text{if } u[j] = 0, \\ u[j]/|u[j]| & \text{else,} \end{cases}$$

where j is the index for the vector component. Because of the value of $\mathrm{sgn}(u)$ where $u[j] = 0$ is arbitrarily selected, such points are points of discontinuity of the sgn function.

In phase retrieval including ptychography, we can write the given data b as

$$(2.7) \qquad b = |u| \quad \text{with} \quad u = Af$$

for some measurement matrix A and unknown object f. For phase retrieval and ptychography, A has some special features described in Appendix A. For most of the subsequent analysis, however, these special features are not relevant.

Let O be the object space, typically a finite-dimensional complex vector space, and $X = AO$. Since the object is a two-dimensional, complex-valued image, we let $O = \mathbb{C}^{n^2}$, where n is the number of pixels in each dimension.

Let N be the total number of data. The data manifold

$$Y := \{u \in \mathbb{C}^N : |u| = b\}$$

is an N (real) dimensional torus. For phase retrieval it is necessary that $N > 2n^2$. Without loss of generality we assume that A has a full rank.

The problem of phase retrieval and ptychography can be formulated as the feasibility problem

$$(2.8) \qquad \text{Find} \quad u \in X \cap Y,$$

in the transform domain $\mathbb{C}^N$ instead of the object domain $\mathbb{C}^{n^2}$.

Let us clarify the meaning of solution in the transform domain since A is overdetermining. Let $\odot$ denote the componentwise (Hadamard) product and we can write

$$(2.9) \qquad P_X u = AA^+ u, P_Y u = b \odot \operatorname{sgn}(u),$$
$$R_X = 2P_X - I, R_Y = 2P_Y - I,$$

where $A^+ := (A^*A)^{-1}A^*$ is the pseudoinverse of A.

We refer to $u = e^{i\alpha}Af, \alpha \in \mathbb{R}$, as the *true* solution (in the transform domain), up to a constant phase factor $e^{i\alpha}$. We say that u is a *generalized solution* (in the transform domain) if

$$|\hat{u}| = b, \quad \hat{u} := P_X u.$$

Accordingly, the alternative (i) in Proposition 2.1 means that if a convex feasibility problem is consistent, then every AAR iterated sequence converges to a generalized solution and hence every fixed point is a generalized solution.

Typically a generalized solution u is neither a feasible solution (since $|u|$ may not equal b) nor unique (since A is overdetermining) and, if $P_X z = 0$, $u + z$ is also a generalized solution. We call u a *regular* solution if u is a generalized solution and $P_X u = u$.

Let $\hat{u} = P_X u$ for a generalized solution u. Since $P_X \hat{u} = \hat{u}$ and $|\hat{u}| = b$, $\hat{u}$ is a regular solution. Let us state this simple fact for easy reference.

Proposition 2.2. *If u is a generalized solution, then $P_X u$ is a regular solution.*

The goal of the inverse problem (2.7) is the unique determination of f, up to a constant phase factor, from the given data b. In other words, uniqueness holds if, and only if, all regular solutions $\hat{u}$ have the form

$$(2.10) \qquad \hat{u} = e^{i\alpha}Af$$

or equivalently, any generalized solution u is an element of the $(2N-2n^2)$-dimensional manifold

$$(2.11) \qquad \{e^{i\alpha}Af - z : P_X z = 0, \ z \in \mathbb{C}^N, \ \alpha \in \mathbb{R}\}.$$

In the transform domain, the uniqueness is characterized by the uniqueness of the regular solution, up to a constant phase factor. Geometrically, uniqueness means that the intersection $X \cap Y$ is a circle (parametrized $e^{i\alpha}$ times Af).

As proved in [9], when the uniqueness (2.11) holds, the fixed point set of the AAR map (2.2) is exactly the continuum set

$$(2.12) \qquad \{u = e^{i\alpha}Af - z : P_X z = 0, \ \operatorname{sgn}(u) = \alpha + \operatorname{sgn}(Af), \ z \in \mathbb{C}^N, \alpha \in \mathbb{R}\}.$$

In (2.12), the phase relation $\operatorname{sgn}(u) = \alpha + \operatorname{sgn}(Af)$ implies that $z = \eta \odot \operatorname{sgn}(u), \eta \in \mathbb{R}^N, b + \eta \geq 0$. So the set (2.12) can be written as

$$(2.13) \qquad \{e^{i\alpha}(b - \eta) \odot \operatorname{sgn}(Af) : P_X(\eta \odot \operatorname{sgn}(Af)) = 0, \ b + \eta \geq 0, \ \eta \in \mathbb{R}^N, \alpha \in \mathbb{R}\},$$

which is an $(N - 2n^2)$ real-dimensional set, a much larger set than the circle $\{e^{i\alpha}Af : \alpha \in \mathbb{R}\}$ for a given f. On the other hand, the fixed point set (2.13) is N-dimensional lower than the set (2.11) of generalized solutions.

A more intuitive characterization of the fixed points can be obtained by applying R_X to the set (2.13). Since

$$R_X[e^{i\alpha}(b-\eta) \odot \operatorname{sgn}(Af)] = e^{i\alpha}(b+\eta) \odot \operatorname{sgn}(Af)$$

amounting to the sign change in front of η, the image set of (2.13) under the map R_X is

$$(2.14) \qquad \{e^{i\alpha}(b+\eta) \odot \operatorname{sgn}(Af) : P_X(\eta \odot \operatorname{sgn}(Af)) = 0, \ b+\eta \geq 0, \ \eta \in \mathbb{R}^N, \alpha \in \mathbb{R}\}.$$

The set (2.14) is the fixed point set of the alternative form of AAR:

$$(2.15) \qquad x_{k+1} = \frac{1}{2}x_k + \frac{1}{2}R_X R_Y x_k$$

in terms of $x_k := R_X u_k$. The expression (2.14) says that the fixed points of (2.15) are generalized solutions with the "correct" Fourier phase.

However, the boundary points of the fixed point set (2.14) are degenerate in the sense that they have vanishing components, i.e., $(b+\eta)[j] = 0$ for some j, and can slow down convergence [24]. Such points are points of discontinuity of the AAR map (2.15) because they are points of discontinuity of $P_Y = b \odot \operatorname{sgn}(\cdot)$ (see also the comment below (3.15)). Indeed, even though AAR converges linearly in the vicinity of the true solution, numerical evidence suggests that globally (starting with a random initial guess) AAR converges sublinearly (cf. [29, 2]). Due to the nonuniformity of convergence, the additional step of applying P_X (Proposition 2.1(i)) at the "right timing" of the iterated process can jumpstart the geometric convergence regime [9].

3. Douglas–Rachford splitting. DRS is an optimization method for solving the following minimization problem:

$$(3.1) \qquad \min_u K(u) + L(u),$$

where the loss functions L and K represent the data constraint Y and the object constraint X, respectively.

To deal with the divergence behavior of AAR (Proposition 2.1(ii)) in the case of, e.g., noisy data, we consider the Poisson log-likelihood cost functions [52, 6]

$$(3.2) \qquad \text{Poisson:} \quad L(u) = \sum_i |u[i]|^2 - b^2[i] \ln |u[i]|^2$$

based on the maximum likelihood principle for the Poisson noise model. The Poisson noise is the most prevalent noise in X-ray coherent diffraction. There is, however, a disadvantage of working with (3.2), i.e., it has a divergent derivative where $u(i)$ vanishes but $b(i)$ does not. This roughness can be softened by considering an asymptotic form

$$(3.3) \qquad \text{Gaussian:} \quad L(u) = \frac{1}{2}|||u| - b||^2.$$

In Appendix B, we show that the Poisson log-likelihood function (3.2) is asymptotically reducible to (3.3). With the constraint $u = Ag$, g is a stationary point in the object domain if and only if

$$g = A^*[\operatorname{sgn}(Ag) \odot b].$$

In the noiseless case, $|Af| = b$ and hence f is a stationary point by the isometry of A. On the other hand, with noisy data there is no regular solution to $|Ax| = b$ with high probability

(since A has many more rows than columns) and f is unlikely to be a stationary point (since the stationarity equation imposes extra constraints on noise).

Moreover, the Hessian of (3.3) at $u = Af$ is positive semi-definite and has one-dimensional eigenspace spanned by if associated with eigenvalue zero [9, 10, 11].

Expanding the loss function (3.3)

$$(3.4) \qquad L(u) = \frac{1}{2}\|u\|^2 - \sum_j b[j]|u[j]| + \frac{1}{2}\|b\|^2$$

we see that L has a *bounded* subdifferential where $u[j]$ vanishes but $b[j]$ does not. There are various tricks to further smooth out (3.3), e.g., by introducing an additional regularization parameter as

$$(3.5) \qquad L(u) = \frac{1}{2}\|\sqrt{|u|^2 + \epsilon} - \sqrt{b^2 + \epsilon}\,\|^2, \quad \epsilon > 0$$

(see, e.g., [8]).

Besides the Poisson noise, a type of noise due to interference from multiple scattering can be modeled as complex circularly symmetric Gaussian noise, resulting in the signal model

$$(3.6) \qquad b = |Af + \eta|,$$

where η is a complex circularly symmetric Gaussian noise. Squaring the expression, we obtain

$$b^2 = |Af|^2 + |\eta|^2 + 2\Re(\overline{\eta} \odot Af).$$

Suppose $|\eta| \ll |Af|$ so that $|\eta|^2 \ll 2\Re(\overline{\eta} \odot Af)$. Then

$$(3.7) \qquad b^2 \approx |Af|^2 + 2\Re(\overline{\eta} \odot Af).$$

Equation (3.7) says that at the photon counting level, the noise appears additive and Gaussian but with variance proportional to $|Af|^2$, the Poisson noise in the asymptotic regime discussed in Appendix B. Therefore the loss function (3.3) is suitable for this case too.

The maximum likelihood scheme is a variance stabilization scheme which uniformizes the probability distribution for every pixel regardless of the measured intensity value [31]. See [28, 56] for more choices of loss functions.

The amplitude-based Gaussian loss function (3.3) is well known to outperform the intensity-based loss function $\frac{1}{2}\||u|^2 - b^2\|^2$, even though the latter is more smooth [55]. Due to the nondifferentiability of both K and L, the global convergence property of the proposed DRS optimization is beyond the current framework of analysis [33]. The ptychographic iterative engines PIE [21, 22, 48], ePIE [40], and rPIE [38], are also related to the minibatch gradient method for the amplitude-based cost function (3.3).

For K, we let $K(u)$ be the indicator function of the range of A, i.e., a "hard" constraint.

When the corresponding feasibility problem is consistent (feasible), there exist $u \in \mathbb{C}^N$ such that $|u| = b$ and $u = Ag$ for some $g \in \mathbb{C}^{n^2}$, which are exactly the global minimizers of (3.1), realizing the minimum value 0, as well as the regular solutions defined in section 2.1.

When the corresponding feasibility problem is inconsistent (infeasible), the minimum value of (3.1) is unknown and the global minimizers are harder to characterize.

DRS is based on the proximal operator which is a generalization of projection. The proximal point relative to a function G is given by

$$\mathrm{prox}_G(u) := \underset{x}{\mathrm{argmin}} \, G(x) + \frac{1}{2}\|x - u\|^2.$$

With the loss functions (3.2) or (3.3), P_X is replaced by $P_{K/\rho}$ and P_Y by $P_{L/\rho}$, respectively, with the step size $\gamma = 1/\rho$. The three-step procedure (2.4)–(2.6) is replaced by

$$v_l = \mathrm{prox}_{K/\rho}(u_l); \tag{3.8}$$

$$w_l = \mathrm{prox}_{L/\rho}(2v_l - u_l), \tag{3.9}$$

$$u_{l+1} = u_l + w_l - v_l \tag{3.10}$$

for $l = 1, 2, 3 \ldots$.

For convex optimization, DRS (3.8)–(3.10) is equivalent to ADMM applied to the dual problem to (3.1). In Appendix C, we show that for phase retrieval they are essentially equivalent to each other.

For our choice of K, $\mathrm{prox}_{K/\rho}(u) = P_X u = AA^+ u$ is independent of ρ. This should be contrasted with the choice of the more smooth distance function adopted in [33] for the tractability of convergence analysis (see more discussion in section 10).

If we define the reflector $\mathcal{R}_Y$ corresponding to $\mathrm{prox}_{L/\rho}(u)$ as

$$\mathcal{R}_Y u := 2\,\mathrm{prox}_{L/\rho}(u) - u, \tag{3.11}$$

then we can write the system (3.8)–(3.10) as

$$u_{k+1} = \frac{1}{2}u_k + \frac{1}{2}\mathcal{R}_Y R_X u_k, \tag{3.12}$$

which is equivalent to

$$x_{k+1} = \frac{1}{2}x_k + \frac{1}{2}R_X \mathcal{R}_Y x_k \tag{3.13}$$

in terms of $x_k := R_X u_k$. In other words, the order of carrying out $\mathrm{prox}_{L/\rho}$ and $\mathrm{prox}_{K/\rho}$ does not matter in the current DRS set-up.

For the Gaussian loss function (3.3), the proximal point can be explicitly derived,

$$\mathrm{prox}_{L/\rho}(u) = \frac{1}{\rho+1}b \odot \mathrm{sgn}(u) + \frac{\rho}{\rho+1}u$$

$$= \frac{1}{\rho+1}(b + \rho|u|) \odot \mathrm{sgn}(u),$$

an averaged projection with the relaxation parameter ρ. Now we are ready to give the most compact and explicit representation of the Gaussian DRS map:

$$u_{k+1} = \frac{u_k}{\rho+1} + \frac{\rho-1}{\rho+1}P_X u_k + \frac{1}{\rho+1}P_Y R_X u_k, \tag{3.14}$$

$$:= \Gamma(u_k)$$

which can be compared with AAR in the form (2.3).

For the Poisson case the DRS map has a more complicated form,

$$u_{k+1} = \frac{1}{2}u_k - \frac{1}{\rho+2}R_X u_k + \frac{\rho}{2(\rho+2)}\left[|R_X u_k|^2 + \frac{8(2+\rho)}{\rho^2}b^2\right]^{1/2} \odot \mathrm{sgn}\left(R_X u_k\right) \tag{3.15}$$

$$:= \Pi(u_k),$$

where b^2 is the vector with component $b^2[j] = (b[j])^2 \; \forall j$.

Note that $\Gamma(u)$ and $\Pi(u)$ are continuous except where $R_X u$ vanishes but b does not due to arbitrariness of the value of the sgn function at zero.

After the iteration is terminated with the terminal vector u_*, the object estimate is obtained by

$$(3.16) \qquad f_* = A^+ u_*.$$

We shall refer to DRS with the Poisson log-likelihood function (3.15) and the Gaussian version (3.14) by *Poisson-DRS* and *Gaussian-DRS*, respectively. The computation involved in Gaussian-DRS and Poisson-DRS are mostly pixelwise operations (hence efficient) except for the pseudoinverse A^+ which can be computed efficiently (see Appendix A).

In the limiting case of $\rho = 0$, both Gaussian-DRS and Poisson-DRS become the AAR algorithm.

4. Fixed points. For simplicity of presentation, we shall focus on the case of the Gaussian DRS.

By definition, all fixed points u satisfy the equation

$$(4.1) \qquad u = \Gamma(u)$$

and hence after some algebra by (3.14)

$$(4.2) \qquad P_X u + \rho P_X^\perp u = b \odot \text{sgn}(R_X u).$$

The main result of this section is that the iteration of Γ always produces a sequence bounded in norm by

$$\frac{\|b\|}{\min\{\rho, 1\}} \qquad \text{for} \qquad \rho > 0$$

(Theorem 4.6) with slightly better bounds on the fixed points (Corollary 4.7). Therefore, Gaussian-DRS is free of the divergence problem associated with AAR in the infeasible case.

It is often convenient to perform the analysis in terms of the pair of variables u and $x := R_X u$. Here are some basic relations between u and x.

Proposition 4.1. *For any $u \in \mathbb{C}^N$, $x := R_X u$ satisfies*

$$u = R_X x, P_X u = P_X x, P_X^\perp u = -P_X^\perp x.$$

Proof. First note that

$$R_X x = 2 P_X x - x = 2 P_X u - (2 P_X u - u) = u.$$

Moreover,

$$P_X x = P_X R_X u = P_X (2 P_X u - u) = 2 P_X u - P_X u = P_X u$$

and

$$P_X^\perp x = x - P_X x = 2 P_X u - u - P_X x = 2 P_X u - u - P_X u = P_X u - u = -P_X^\perp u. \qquad \blacksquare$$

Proposition 4.2. *Any $u \in \mathbb{C}^N$ is a generalized solution if and only if $x := R_X u$ is a generalized solution.*

Proof. If u is a generalized solution, then $P_X u = P_X x$ by Proposition 4.1. Now that x is a generalized solution, the converse is also true by the same argument. ∎

Proposition 4.3. *If u is a generalized solution, then $P_X u$ is a regular solution and a fixed point.*

Proof. Let $\hat{u} = P_X u$. By Proposition 2.2 $\hat{u}$ is a regular solution. Moreover $\Gamma(u)$ becomes

$$\frac{1}{2}\hat{u} + \frac{\rho - 1}{2(\rho + 1)}\hat{u} + \frac{1}{\rho + 1} b \odot \mathrm{sgn}(\hat{u}) = \frac{1}{2}\hat{u} + \frac{\rho - 1}{2(\rho + 1)}\hat{u} + \frac{1}{\rho + 1}\hat{u},$$

which equals $\hat{u}$. Therefore $\hat{u}$ is a fixed point. ∎

Proposition 4.4. *Suppose $P_X u = u$. Then u is a regular solution if, and only if, u is a fixed point.*

Proof. Under the assumption $P_X u = u$, $u = R_X u$ and $\Gamma(u)$ becomes

$$(4.3) \qquad \frac{1}{2}u + \frac{\rho - 1}{2(\rho + 1)}u + \frac{1}{\rho + 1} b \odot \mathrm{sgn}(u) = \frac{\rho}{1 + \rho}u + \frac{1}{\rho + 1} b \odot \mathrm{sgn}(u).$$

Therefore, if u is a fixed point, then (4.2) implies

$$u = b \odot \mathrm{sgn}(u)$$

and hence $|u| = b$, i.e., u is a regular solution.

On the other hand, if $|u| = b$, then the right-hand side of (4.3) becomes

$$\frac{\rho}{1 + \rho}u + \frac{1}{\rho + 1} b \odot \mathrm{sgn}(u) = \frac{\rho}{1 + \rho}u + \frac{1}{\rho + 1}u = u,$$

implying that u is a fixed point. ∎

Writing

$$I = P_X + P_X^\perp \quad \text{and} \quad R_X = P_X - P_X^\perp$$

and using Proposition 4.1 we can put the Gaussian-DRS map and the fixed point equation in the following forms.

Proposition 4.5. *The Gaussian-DRS map Γ is equivalent to*

$$(4.4) \qquad P_X u_{k+1} = \frac{\rho}{\rho + 1} P_X u_k + \frac{1}{\rho + 1} P_X P_Y x_k,$$

$$(4.5) \qquad P_X^\perp u_{k+1} = \frac{1}{\rho + 1} P_X^\perp u_k + \frac{1}{\rho + 1} P_X^\perp P_Y x_k,$$

where $x_k := R_X u_k$. Therefore any fixed point u satisfies

$$(4.6) \qquad P_X x = P_X P_Y x,$$
$$(4.7) \qquad -\rho P_X^\perp x = P_X^\perp P_Y x,$$

where $x := R_X u$, *or equivalently*

$$(4.8) \qquad P_X x - \rho P_X^\perp x = b \odot \mathrm{sgn}(x),$$

$$(4.9) \qquad P_X x + \rho P_X^\perp x = R_X \left(b \odot \mathrm{sgn}(x) \right).$$

Next we show that the Gaussian-DRS map Γ with $\rho > 0$ always produces a bounded iterated sequence, in contrast to the divergence behavior of AAR given in Proposition 2.1(ii).

Theorem 4.6. *Let* $u_{k+1} := \Gamma(u_k)$, $k \in \mathbb{N}$, *and* $x_k := R_X u_k$. *Then, for* $\rho > 0$, $\{u_k\}$ *and* $\{x_k\}$ *are bounded sequences. Moreover,*

$$(4.10) \qquad \limsup_{k\to\infty} \|u_k\| = \limsup_{k\to\infty} \|x_k\| \le \frac{\|b\|}{\min\{\rho, 1\}} \quad for \quad \rho > 0$$

and hence all fixed points u *satisfy*

$$(4.11) \qquad \|u\| \le \frac{\|b\|}{\min\{\rho, 1\}} \quad for \quad \rho > 0.$$

Proof. Since P_X is an orthogonal projection, we have

$$\|x_k\| = \|u_k\| = \sqrt{\|P_X x_k\|^2 + \|P_X^\perp x_k\|^2}.$$

By Proposition 4.5 we then have the estimates

$$(4.12) \qquad \|u_{k+1}\| \le \left\| \frac{1}{\rho+1} P_X^\perp u_k + \frac{\rho}{\rho+1} P_X u_k \right\| + \frac{1}{\rho+1} \|P_Y x_k\|$$

$$= \left[\frac{1}{(\rho+1)^2} \|P_X^\perp u_k\|^2 + \frac{\rho^2}{(\rho+1)^2} \|P_X u_k\|^2 \right]^{1/2} + \frac{1}{\rho+1} \|P_Y x_k\|$$

$$\le \frac{\max\{\rho, 1\}}{\rho+1} \|u_k\| + \frac{1}{\rho+1} \|b\|.$$

Hence, iterating (4.12) for $\rho \ge 1$ we obtain

$$\|u_{k+1}\| \le \frac{\rho^k}{(\rho+1)^k} \|u_1\| + \frac{\|b\|}{\rho+1} \sum_{j=0}^{k-1} \frac{\rho^j}{(1+\rho)^j}$$

and, after passing to the limit, the upper bound (4.10).

On the other hand, for $\rho < 1$,

$$\|u_{k+1}\| \le \frac{1}{(\rho+1)^k} \|u_1\| + \|b\| \sum_{j=1}^{k} \frac{1}{(\rho+1)^j}$$

implying (4.10). ∎

We can improve (4.11) slightly by Proposition 4.5.

Corollary 4.7. *For any fixed point u, let $x := R_X u$. Then*

$$\|u\| = \|x\| < \|b\| \quad if \quad \rho > 1 \tag{4.13}$$

and

$$\|b\| < \|u\| = \|x\| \leq \|b\|/\rho \quad if \quad \rho \in (0,1) \tag{4.14}$$

unless $P_X x = x$ (or equivalently $P_X u = u$), in which case $u = x$ is a regular solution. On the other hand, for $\rho = 1$, $\|u\| = \|x\| = \|b\|$ for any fixed point u.

Proof. By (4.8) and that P_X is an orthogonal projection, we have

$$\|P_X x\|^2 + \rho \|P_X^\perp x\|^2 = \|b\|^2, \tag{4.15}$$

which implies

$$\|u\| = \|x\| \begin{cases} < \|b\| & \text{for} \quad \rho > 1 \\ > \|b\| & \text{for} \quad \rho < 1 \end{cases} \quad \text{if} \quad \|P_X^\perp x\| \neq 0. \tag{4.16}$$

If $\|P_X^\perp x\| = 0$, then $x = P_X x$ and (4.8) becomes $x = b \odot \mathrm{sgn}(x)$, implying $|x| = b$. Likewise, $x = P_X x$ implies that $u = x$.

Moreover, by (4.11), $\|u\| = \|x\| \leq \|b\|/\rho$ for $\rho \in (0,1)$. Hence (4.16) can be further strengthened to the statement (4.13)–(4.14).

For $\rho = 1$, (4.15) implies that $\|x\| = \|b\|$. ∎

In Appendix D we give a perturbation analysis for the similar result in the Poisson case with small ρ.

5. Stability analysis. When the uniqueness (2.11) holds, the fixed point set of AAR ($\rho = 0$) is explicitly given in (2.12). For $\rho > 0$, the fixed point set is much harder to characterize explicitly. Instead, we show that the desirable fixed points (i.e., regular solutions) are automatically distinguished from the other nonsolutional fixed points by their stability type.

We say that a fixed point is *attracting* if the spectral radius of the subdifferential map is at most 1 and *nonattracting* if otherwise. Because a constant phase factor is an inherent ambiguity, any reasonable iterative map has at least one-dimensional *center manifold*. We say that a fixed point is *strictly attracting* if the center manifold is one-dimensional, i.e., a positive spectral gap between the second singular value of the subdifferential map and 1 (see section 6).

Roughly speaking, we shall prove that for $\rho \geq 1$ all attracting fixed points must be regular solutions (Theorem 5.2) and that for $\rho \geq 0$ all regular solutions are attracting (Theorem 5.4). In other words, for $\rho \geq 1$, we need not be concerned with the problem of stagnation near a fixed point that is not a regular solution (a common problem with AP). Moreover, we know that the regular solutions are strictly attracting under additional mild conditions (Corollary 6.2). On the other hand, the problem of divergence (associated with AAR) when the data constraint is infeasible does not arise for Gaussian-DRS in view of Theorem 4.6.

Proposition 5.1. *Let $x := R_X u$ and assume $|x| > 0$. Set*

$$(5.1) \qquad \Omega = \mathrm{diag}(\mathrm{sgn}(x)), \quad \tilde{P}_X = \Omega^* P_X \Omega, \quad \tilde{R}_X = \Omega^* R_X \Omega.$$

Then

$$\lim_{\epsilon \to 0} \Omega^* (\Gamma(u + \epsilon v) - \Gamma(u))/\epsilon = J_A(\eta), \quad \eta = \Omega^* v,$$

where

$$(5.2) \qquad J_A(\eta) = \frac{1}{2}\eta + \frac{\rho - 1}{2(\rho + 1)} \tilde{R}_X \eta + \frac{\mathrm{i}}{\rho + 1} \frac{b}{|x|} \odot \Im \left[\tilde{R}_X \eta \right].$$

Proof. The key observation is that the derivative of $\mathrm{sgn}(c) = c/|c| \in \mathbb{C}, c \neq 0$, is given by

$$\begin{aligned} \lim_{\epsilon \to 0} \frac{1}{\epsilon} \left[\frac{c + \epsilon a}{|c + \epsilon a|} - \frac{c}{|c|} \right] &= \lim_{\epsilon \to 0} \frac{\mathrm{sgn}(c)}{\epsilon} \left[\frac{1 + \epsilon a/c}{|1 + \epsilon a/c|} - 1 \right] \\ &= \mathrm{i} \Im \left[a/c \right] \mathrm{sgn}(c) \\ &= \mathrm{i} \Im \left[\mathrm{sgn}(\bar{c}) a \right] \frac{\mathrm{sgn}(c)}{|c|} \end{aligned}$$

for any $a \in \mathbb{C}$, where $\Im$ denotes the imaginary part. So we have

$$\lim_{\epsilon \to 0} \frac{1}{\epsilon} (\Gamma(u + \epsilon v) - \Gamma(u)) = \frac{1}{2}v + \frac{\rho - 1}{2(\rho + 1)} R_X v + \frac{\mathrm{i}}{\rho + 1} \frac{b}{|x|} \odot \Omega \Im \left[\Omega^* R_X v \right],$$

which, in terms of $\eta = \Omega^* v$ and the notation (5.1), becomes Ω times J_A in (5.2). ∎

The following result says that for $\rho \geq 1$ all the nonsolution fixed points are nonattracting.

Theorem 5.2. *Let $\rho \geq 1$. Let u be a fixed point such that $x := R_X u$ has no vanishing components. Suppose*

$$(5.3) \qquad \|J_A(\eta)\| \leq \|\eta\| \quad \forall \eta \in \mathbb{C}^N.$$

Then

$$(5.4) \qquad x = P_X x = b \odot \mathrm{sgn}(x),$$

implying $u = x$ is a regular solution.

Remark 5.3. Previous results [9] suggest that when the regular solution is unique up to a constant factor, all AAR fixed points in (2.14) are attracting in the sense (5.3). In other words, Theorem 5.2 is likely false for $\rho = 0$.

Proof. In view of Proposition 4.5, it suffices to show that $P_X^\perp x = 0$.
We prove the statement by contradiction. Suppose $P_X^\perp x \neq 0$.
By (4.8) and the Pythogoras theorem we have

$$(5.5) \qquad \|P_X x\|_2^2 + \rho^2 \|P_X^\perp x\|^2 = \|b\|^2$$

and hence $\|b\| \geq \|x\|$ for $\rho \geq 1$. Applying Ω^* we rewrite (4.9) as

$$\tilde{P}_X|x| + \rho(|x| - \tilde{P}_X|x|) = \tilde{R}_X b. \tag{5.6}$$

On the other hand, applying $\tilde{P}_X$ on (5.6) we have

$$\tilde{P}_X|x| = \tilde{P}_X b$$

and hence by (5.6)

$$\tilde{P}_X|x| = \tilde{P}_X b = \frac{\rho|x|}{1+\rho} + \frac{b}{1+\rho}. \tag{5.7}$$

We now show that $\|J_A(\eta)\| > \|\eta\|$ for any η such that

$$\tilde{R}_X \eta = \mathrm{i}\tilde{P}_X b = \frac{\mathrm{i}\rho}{1+\rho}|x| + \frac{\mathrm{i}}{1+\rho}b. \tag{5.8}$$

To this end, it is more convenient to write J_A in (5.2) in terms $\xi := \tilde{R}_X \eta$. With a slight abuse of notation we write

$$J_A(\xi) = \tilde{P}_X \xi - \frac{\xi}{\rho+1} + \frac{\mathrm{i}}{\rho+1}\frac{b}{|x|} \odot \Im(\xi), \tag{5.9}$$

where we have used the properties in Proposition 4.1.

Since $\|\xi\| = \|\eta\|$, our goal is to show $\|J_A(\xi)\| > \|\xi\|$.

First we make an observation that will be useful later. We claim that

$$\rho\|x\|^2 = \|b\|^2 + (\rho-1)|x| \cdot b, \tag{5.10}$$

where "·" denotes the (real) scalar product between two vectors. By (5.7),

$$\tilde{P}_X^{\perp} b = b - \tilde{P}_X b = \frac{\rho}{1+\rho}(|b| - |x|),$$

and hence by the Pythogoras theorem

$$\begin{aligned}
\|b\|^2 &= \|\tilde{P}_X b\|^2 + \|\tilde{P}_X^{\perp} b\|^2 \\
&= \left\| \frac{\rho|x|}{1+\rho} + \frac{b}{1+\rho} \right\|^2 + \left\| \frac{\rho}{1+\rho}(|b| - |x|) \right\|^2 \\
&= \frac{2\rho^2}{(\rho+1)^2}\|x\|^2 + \frac{2\rho(1-\rho)}{(\rho+1)^2}|x| \cdot b + \frac{\rho^2+1}{(\rho+1)^2}\|b\|^2,
\end{aligned}$$

which becomes (5.10) after rearrangement.

Next, note that by (5.8)

$$\tilde{P}_X \xi = \tilde{P}_X \eta = \mathrm{i}\tilde{P}_X b = \xi,$$

which is purely imaginary, and hence

$$J_A(\xi) = \frac{\rho}{\rho+1}\xi + \frac{\mathrm{i}}{\rho+1}\frac{b}{|x|} \odot \xi \tag{5.11}$$

by (5.9).

After some tedious but straightforward algebra with (5.8) and (5.11), we see that $\|J_A(\xi)\| > \|\xi\|$ is equivalent to the inequality

$$0 < (5\rho^2 - 2\rho - 1)\|b\|^2 + (2\rho^3 - 4\rho^2 - 2\rho)|x| \cdot b + 4\rho \frac{b}{|x|} \cdot b^2 + \left\|\frac{b^2}{|x|}\right\|^2 - \rho^2(2\rho + 1)\|x\|^2,$$

which by (5.10) reduces to

$$(5.12) \qquad 0 < (3\rho^2 - 3\rho - 1)\|b\|^2 - (3\rho^2 + \rho)|x| \cdot b + 4\rho \frac{b}{|x|} \cdot b^2 + \left\|\frac{b^2}{|x|}\right\|^2.$$

To proceed, we note that the assumption $\tilde{P}_X^\perp x \neq 0$ implies $|x| \neq b$, $\|x\| < \|b\|$ and moreover $|x|, b$ are not a multiple of each other. So by the Cauchy–Schwarz inequality we have

$$\left\|\frac{b^2}{|x|}\right\| > \frac{\|b\|^2}{\|x\|},$$

$$\frac{b}{|x|} \cdot b^2 = \left\|\frac{b^{3/2}}{|x|^{1/2}}\right\|^2 > \frac{\|b\|^4}{\||x|^{1/2} \odot b^{1/2}\|^2} = \frac{\|b\|^4}{|x| \cdot b},$$

and hence the last two terms on the right-hand side of (5.12) have the strict lower bound

$$(5.13) \qquad 4\rho \frac{b}{|x|} \cdot b^2 + \left\|\frac{b^2}{|x|}\right\|^2 > 4\rho \frac{\|b\|^4}{|x| \cdot b} + \frac{\|b\|^4}{\|x\|^2}$$
$$> (1 + 4\rho)\|b\|^2,$$

where we have used the fact $\|b\| \geq \|x\|$ due to $\rho \geq 1$.

In view of (5.13) the right-hand side of (5.12) is strictly greater than

$$(3\rho^2 - 3\rho - 1)\|b\|^2 - (3\rho^2 + \rho)\|b\|^2 + (1 + 4\rho)\|b\|^2 = 0.$$

In other words, (5.12) holds indeed and the proof for $\|J_A(\xi)\| > \|\xi\|$ is complete.

This clearly contradicts the assumption (5.3). Therefore, $P_X^\perp x = 0$ and the desired result (5.4) follows from Propositions 4.4 and 4.5. ∎

The next result says that for any $\rho \geq 0$, all regular solutions are attracting fixed points.

Theorem 5.4. *Let $\rho \geq 0$. Let u be a nonvanishing regular solution. Then*

$$(5.14) \qquad \|J_A(\eta)\| \leq \|\eta\|$$

$\forall \eta \in \mathbb{C}^N$ *and the equality holds in the direction $\pm$ib (and possibly elsewhere on the unit sphere).*

Proof. By Proposition 4.4, $x := R_X u = u$ is a fixed point. By Proposition 4.5,

$$u = b \odot \operatorname{sgn}(u) = Ag \quad \text{for some } g.$$

Rewriting $J_A(\eta)$ in (5.2) as

$$J_A(\eta) = \tilde{P}_X \eta - \frac{1}{\rho + 1}\tilde{R}_X \eta + \frac{\mathrm{i}}{1 + \rho}\frac{b}{|x|} \odot \Im\left(\tilde{R}_X \eta\right)$$

and using $|x| = b$ we obtain

$$J_A(\eta) = \tilde{P}_X \eta - \frac{1}{1+\rho} \Re(\tilde{R}_X \eta),$$

where $\Re$ denotes the real part. We now show that $\|J_A(\eta)\| \le \|\eta\| \ \forall \ \eta$.

To proceed, we shall write $\tilde{P}_X = HH^*$ where H is an isometry. This can be done for the matrix $C := \Omega^* A$ via the QR decomposition. In our setting, the measurement matrix of each diffraction pattern has orthogonal columns and so does the total measurement matrix. Hence the R factor of C is a diagonal matrix with the norms of the columns of C on the diagonal (see Appendix A). For ease of notation, we may assume that $\Omega^* A = H$.

Note that

(5.15)
$$\begin{bmatrix} \Re[H] & -\Im[H] \\ \Im[H] & \Re[H] \end{bmatrix}$$

is real isometric because H is complex isometric. Define

(5.16)
$$\mathcal{H} := \begin{bmatrix} \Re[H] & \Im[H] \end{bmatrix} \in \mathbb{R}^{N \times 2n^2}.$$

As in the set-up detailed in Appendix A let the object be an $n \times n$ square image and $\mathbb{C}^{n^2}$ the object domain.

By Proposition E.4 in Appendix E, HH^* can be block-diagonalized into one $(N - 2n^2) \times (N - 2n^2)$ zero-block and $2n^2$ 2×2 blocks of the form

(5.17)
$$\begin{bmatrix} \lambda_k^2 & \lambda_k \lambda_{2n^2+1-k} \\ \lambda_k \lambda_{2n^2+1-k} & \lambda_{2n^2+1-k}^2 \end{bmatrix}, \quad k = 1, 2, \ldots, 2n^2,$$

in the orthonormal basis $\{\eta_k, \mathrm{i}\eta_{2n^2+1-k} : k = 1, 2, \ldots, 2n^2\}$ where $\eta_k \in \mathbb{R}^N$ are the right singular vectors, corresponding to the singular values λ_k, of $\mathcal{H}$.

Moreover, the complete set of singular values satisfy

(5.18)
$$1 = \lambda_1 \ge \lambda_2 \ge \cdots \ge \lambda_{2n^2} = \lambda_{2n^2+1} = \cdots = \lambda_N = 0,$$

(5.19)
$$\lambda_k^2 + \lambda_{2n^2+1-k}^2 = 1.$$

In view of the block-diagonal nature of HH^*, we shall analyze $J_A(\eta)$ in the 2-dim spaces spanned by the orthonormal basis $\{\eta_k, \mathrm{i}\eta_{2n^2+1-k}\}$ one k at a time.

For any fixed k and any $z_1, z_2 \in \mathbb{C}$ let

$$\eta = z_1 \eta_k + \mathrm{i}z_2 \eta_{2n^2+1-k}$$
$$= \Re[z_1]\eta_k + \Re[z_2]\mathrm{i}\eta_{2n^2+1-k} + \Im[z_1]\mathrm{i}\eta_k - \Im[z_2]\eta_{2n^2+1-k}.$$

We shall use the basis $\{\eta_k, \mathrm{i}\eta_{2n^2+1-k}, \mathrm{i}\eta_k, -\eta_{2n^2+1-k}\}$ for expressing η and $J_A(\eta)$.

We obtain

(5.20)
$$J_A(\eta) = \left(\lambda_k^2 z_1 + \lambda_k \lambda_{2n^2+1-k} z_2\right) \eta_k + \left(\lambda_k \lambda_{2n^2+1-k} z_1 + \lambda_{2n^2+1-k}^2 z_2\right) \mathrm{i}\eta_{2n^2+1-k}$$

$$+ \frac{1}{1+\rho} \left[(1 - 2\lambda_k^2)\Re(z_1) - 2\lambda_k \lambda_{2n^2+1-k}\Re(z_2)\right] \eta_k$$

$$+ \frac{1}{1+\rho} \left[2\lambda_k \lambda_{2n^2+1-k}\Im(z_1) - (1 - 2\lambda_{2n^2+1-k}^2)\Im(z_2)\right] \eta_{2n^2+1-k}.$$

Next we treat (5.20) as a linear function of $\Re(z_1), \Re(z_2), \Im(z_1), \Im(z_2)$ with real coefficients in the basis $\{\eta_k, i\eta_{2n^2+1-k}, i\eta_k, -\eta_{2n^2+1-k}\}$ and represent J_A by a 4×4 matrix which is block-diagonalized into two 2×2 blocks:

$$(5.21) \quad \begin{bmatrix} \frac{1}{1+\rho} + \frac{\rho-1}{\rho+1}\lambda_k^2 & \frac{\rho-1}{\rho+1}\lambda_k\lambda_{2n^2+1-k} \\ \lambda_k\lambda_{2n^2+1-k} & \lambda_{2n^2+1-k}^2 \end{bmatrix}, \quad \begin{bmatrix} \lambda_k^2 & \lambda_k\lambda_{2n^2+1-k} \\ \frac{\rho-1}{\rho+1}\lambda_k\lambda_{2n^2+1-k} & \frac{1}{\rho+1} + \frac{\rho-1}{\rho+1}\lambda_{2n^2+1-k}^2 \end{bmatrix}$$

with the former of (5.21) acting on $\Re(z_1), \Re(z_2)$ and the latter acting on $\Im(z_1), \Im(z_2)$.

The eigenvalues of the matrices in (5.21) are, respectively,

$$(5.22) \quad \frac{1}{2(\rho+1)}\left[\rho + 2\lambda_{2n^2+1-k}^2 \pm \sqrt{\rho^2 - 4\lambda_k^2\lambda_{2n^2+1-k}^2}\right],$$

$$(5.23) \quad \frac{1}{2(\rho+1)}\left[\rho + 2\lambda_k^2 \pm \sqrt{\rho^2 - 4\lambda_k^2\lambda_{2n^2+1-k}^2}\right].$$

Because the two expressions are symmetrical with respect to the exchange of index ($k \leftrightarrow 2n^2+1-k$), it suffices to analyze (5.22), which, with the $+$ sign, equals 1 at $k = 2n^2$ (recall $\lambda_{2n^2} = 0$). Next we show that 1 is the largest eigenvalue among all k and $\rho \in [0, \infty)$.

Note that (5.22) is real-valued for any $\lambda_k \in [0, 1]$ if and only if $\rho \geq 1$. Hence, for $\rho \geq 1$, the maximum eigenvalue is 1 and occurs at $k = 2n^2$.

For $\rho < 1$ and $\rho^2 - 4\lambda_k^2 + 4\lambda_k^4 \geq 0$, the maximum value of (5.22) can be bounded as

$$(5.24) \quad \frac{1}{2(\rho+1)}\left[\rho + 2(1 - \lambda_k^2) + \sqrt{\rho^2 - 4\lambda_k^2(1 - \lambda_k^2)}\right]$$
$$\leq \frac{1}{2(\rho+1)}\left[\rho + 2(1 - \lambda_k^2) + \rho\right]$$
$$= 1 - \frac{\lambda_k^2}{\rho+1} \leq 1$$

since $4\lambda_k^2(1 - \lambda_k^2) \geq 0$. Hence the expression (5.22) achieves the maximum value 1 at $k = 2n^2$.

For $\rho < 1$ and $\rho^2 - 4\lambda_k^2 + 4\lambda_k^4 \leq 0$, the modulus of (5.22) equals

$$(5.25) \quad \sqrt{\frac{1 - \lambda_k^2}{1+\rho}} \leq 1.$$

By Proposition E.1, $\eta_1 = b$, $\tilde{P}_X(ib) = ib$, $\tilde{R}_X(ib) = ib$ and hence $J_A(ib) = ib$. However, $\arg\max_{\|\eta\|=1}|J_A(\eta)|$ may contain points other than $\pm ib/\|b\|$ since we do not know if $\lambda_2 < 1$ without additional conditions (see section 6). The proof is complete. ∎

6. Spectral gap. To derive a positive spectral gap ($\lambda_2 < \lambda_1 = 1$), we need some details of the ptychographic set-up (Appendix A).

Let $\mathcal{T}$ be the set of all shifts, including $(0, 0)$, involved in the ptychographic measurement. Denote by $\mu^{\mathbf{t}}$ the $\mathbf{t}$-shifted probe $\forall \mathbf{t} \in \mathcal{T}$ and $\mathcal{M}^{\mathbf{t}}$ the domain of $\mu^{\mathbf{t}}$. Let $f^{\mathbf{t}}$ be the object restricted to $\mathcal{M}^{\mathbf{t}}$. For convenience, we assume the periodic boundary condition on the whole object domain $\mathcal{M} = \cup_{\mathbf{t}\in\mathcal{T}}\mathcal{M}^{\mathbf{t}}$ when $\mu^{\mathbf{t}}$ crosses over the boundary of $\mathcal{M}$.
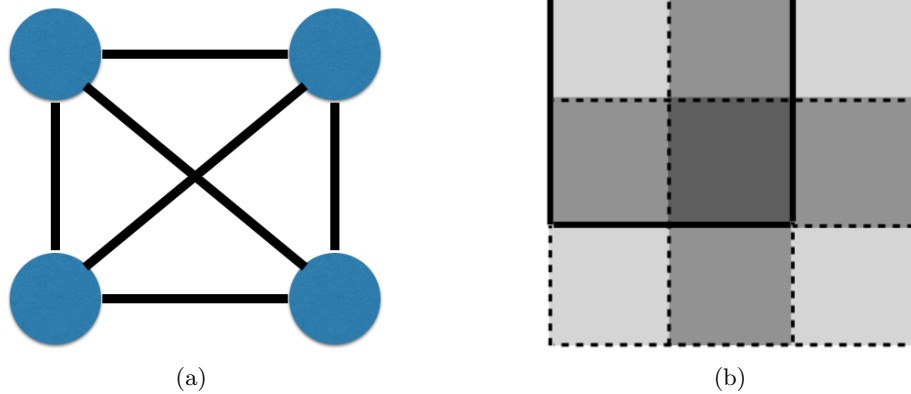
Figure 2. *A complete undirected graph* (a) *representing four connected object parts* (b) *where the gray level indicates the number of coverages by the mask in four scan positions.*

Two blocks $\mathcal{M}^{\mathbf{t}}$ and $\mathcal{M}^{\mathbf{t}'}$ are said to be connected if the minimum overlap condition

$$\#\{\mathcal{M}^{\mathbf{t}} \cap \mathcal{M}^{\mathbf{t}'} \cap \mathrm{supp}(f)\} \geq 2$$

is satisfied. Let $\mathcal{G}$ be the undirected graph with the nodes corresponding to $\{\mathcal{M}^{\mathbf{t}} : \mathbf{t} \in \mathcal{T}\}$ and the edges between any pair of connected nodes (see Figure 2).

Now we recall the following spectral gap theorem [10] (Proposition 3.5 and the subsequent remark).

Proposition 6.1 (see [10]). *In addition to the above assumptions, suppose* $\mathrm{supp}(f)$ *is not a subset of a line. Let u (and hence $x := R_X u$) be a regular solution. Let λ_2 be the second largest singular value of $\mathcal{H}$ defined in* (5.16). *If the graph $\mathcal{G}$ is connected, then $\lambda_2 < 1$.*

Some theoretical bounds for λ_2 can be found in [10].

Using Proposition 6.1, we can sharpen the result of Theorem 5.4 as follows.

Corollary 6.2. *Under the assumptions of Proposition* 6.1, *the second largest singular value of J_A is strictly less than* 1 *and achieves the minimum value*

$$(6.1) \qquad \frac{\lambda_2}{\sqrt{1+\rho_*}} \quad at \quad \rho_* = 2\lambda_2\sqrt{1-\lambda_2^2} \in [0,1].$$

Moreover, the second largest singular value of J_A is an increasing function of ρ in the range $[\rho_*, \infty)$ and a decreasing function in the range of $[0, \rho_*]$.

Remark 6.3. By arithmetic-geometric-mean inequality,

$$\rho_* \leq 2 \times \frac{1}{2}\sqrt{\lambda_2^2 + 1 - \lambda_2^2} = 1,$$

where the equality holds only when $\lambda_2^2 = 1/2$.

As λ_2^2 tends to 1, ρ_* tends to 0, and as λ_2^2 tends to $\frac{1}{2}$, ρ_* tends to 1. Recall that $\lambda_2^2 + \lambda_{2n^2-1}^2 = 1$ and hence $[1/2, 1]$ is the proper range of λ_2^2.

Proof. Our discussion splits into several cases. By the identity $\lambda_2^2 = 1 - \lambda_{2n^2-1}^2$, we have $\lambda_2^2(1 - \lambda_2^2) = \lambda_{2n^2-1}^2(1 - \lambda_{2n^2-1}^2)$ and $\lambda_2^2 \geq 1/2$.

For $\rho > 1$, the larger eigenvalue in (5.22) achieves the second largest value

$$(6.2) \qquad \frac{1}{2(1+\rho)}\left[\rho + 2\lambda_2^2 + \sqrt{\rho^2 - 4\lambda_2^2(1 - \lambda_2^2)}\right]$$

at $k = 2n^2 - 1$ after some algebra. The expression (6.2) is strictly less than

$$\frac{1}{2(1+\rho)}\left[2\rho + 2\lambda_2^2\right] = \frac{\rho + \lambda_2^2}{\rho + 1} < 1$$

with the spectral gap $\lambda_2 < 1$.

For $\rho = 1$, (5.22) becomes

$$\frac{1}{4}\left[1 + 2(1 - \lambda_k^2) \pm |1 - 2\lambda_k^2|\right],$$

which achieves the second largest value

$$(6.3) \qquad 1 - \lambda_{2n^2-1}^2 = \lambda_2^2 < 1$$

at $k = 2n^2 - 1$ by (5.19).

The case of $\rho < 1$ requires more analysis since the eigenvalue (5.22) may be real or complex. Analyzing as in (5.24) and (5.25) we conclude that the second largest value is

$$(6.4) \qquad \frac{1}{2(\rho+1)}\left[\rho + 2\lambda_2^2 + \sqrt{\rho^2 - 4\lambda_2^2(1 - \lambda_2^2)}\right] \quad \text{if} \quad \rho \geq \rho_* = 2\lambda_2\sqrt{1 - \lambda_2^2}$$

and

$$(6.5) \qquad \frac{\lambda_2}{\sqrt{1+\rho}} \quad \text{if} \quad \rho \leq \rho_*.$$

While the expression in (6.5) is a decreasing function of ρ and less than λ_2, (6.4) is an increasing function of ρ and less than (6.3) for $\rho = 1$.

Also, for $\rho > 1$, the expression (6.2), as a function of ρ, has the derivative

$$\frac{1}{2(\rho+1)^2}\left[1 - 2\lambda_2^2 + \frac{\rho + 4\lambda_2^2(1 - \lambda_2^2)}{\sqrt{\rho^2 - 4\lambda_2^2(1 - \lambda_2^2)}}\right] > \frac{1}{2(\rho+1)^2}\left[2 - 2\lambda_2^2\right] > 0$$

and hence achieves the minimum at $\rho = 1$. In other words, Gaussian-DRS with $\rho = 1$ converges faster than Gaussian-DRS with $\rho > 1$.

From the preceding analysis, the second largest singular value achieves the minimum at the crossover value ρ_* of the two expressions in (6.4). Substituting ρ_* in (6.4) we arrive at (6.1).

Although it is not immediately obvious, it can be verified by elementary (but somewhat tedious) calculus that (6.1) is less than λ_2^2 (for $\rho = 1$). ∎

For comparison with AAR, we note that, for $\rho = 0$, (6.5) is exactly λ_2 and hence greater than λ_2^2 in (6.3), the convergence rate for $\rho = 1$, which coincides with the convergence rate of AP [11]. We state this observation as a corollary.

Corollary 6.4. *For the Gaussian-DRS with $\rho = 1$, the local convergence rate is given by λ_2^2, which is smaller than the convergence rate λ_2 for $\rho = 0$.*

With a positive spectral gap, this largest eigenvalue 1 in Theorem 5.4 corresponds to the global phase factor and Corollary 6.2 can be used to prove local, linear convergence for Gaussian-DRS with $\rho \geq 0$. The proof is analogous to that in [10] for phase retrieval (Theorem 5.1) and in [9] (Theorem 3.4) for ptychography for AAR ($\rho = 0$). But the argument is technical in nature and omitted here for the sake of space.

7. Selection of parameter. A goal of the present work is to circumvent the divergence behavior of AAR (as stated in Proposition 2.1(ii) for the convex case) when the feasibility problem is inconsistent and has no (generalized or regular) solution.

Let us first examine how this problem manifests in the fixed point equation (4.2) reproduced here for the convenience of the reader:

$$P_X u + \rho P_X^\perp u = b \odot \operatorname{sgn}(R_X u).$$

For $\rho = 0$, $P_X u = b \odot \operatorname{sgn}(R_X u)$ and, in particular, $|P_X u| = b$, i.e., every fixed point of AAR is a generalized solution. So if the problem is inconsistent, then no solution (generalized or regular) exists, implying the fixed point set is empty.

The case with $\rho > 0$ is harder to analyze. For $\rho \geq 1$, however, Theorem 5.2 says that all attracting fixed points are regular solutions and hence in the inconsistent case all fixed points are repelling in some directions (likely partially hyperbolic with a center manifold containing at least a circle corresponding to an arbitrary constant phase factor). In other words convergence to a fixed point is almost impossible in the inconsistent case with $\rho \geq 1$. From this perspective, Theorem 5.2 is a pessimistic result in the traditional sense of convergence analysis.

But all hope is not lost. First of all, let us recall the earlier observation that in the inconsistent case, f is probably not a stationary point of the loss function. Hence, a convergent iterative scheme to a stationary point may not be a good idea after all. A good iterative scheme need not converge as long as it produces a good outcome when properly terminated, i.e., its iterates stay in the true solution's vicinity of size comparable to the noise level.

Second, Theorem 4.6 implies that every Gaussian-DRS sequence is bounded and has a convergent subsequence $\{u_{k_j}\}_{j=1}^\infty$ with the limit, say, $\hat{u}$. If, in addition,

$$(7.1) \qquad\qquad \lim_{j \to \infty} (u_{k_j} - \Gamma(u_{k_j})) = 0,$$

then by taking the limit on both sides of the fixed point equation (4.2), one can conclude that $\hat{u}$ is a fixed point. The preceding analysis tells us that in the inconsistent case (7.1) is false for $\rho \geq 1$ (the case with $\rho \in (0, 1)$ is open), suggesting that $\hat{u}$ is part of a more complicated attractor.

In particular, if $\hat{x} := R_X \hat{u}$ does not vanish where $b > 0$, then, by the continuity of Γ at such points, $\hat{u}_1 := \lim_j \Gamma(u_{k_j})$ exists. Assuming that $R_X \Gamma^l(u_{k_j}), l \geq 1$, do not vanish wherever $b > 0$, we obtain a set of cluster points $\hat{u}_l = \lim_j \Gamma^l(u_{k_j}), l \geq 1$, which constitutes a new iterated sequence, i.e., $\hat{u}_{l+1} = \Gamma(\hat{u}_l)$. This is the case of limit cycle in theory of bifurcation. If, however, the nonvanishing assumption fails, then different orbits can branch off at discontinuities.

(a) (b)

Figure 3. (a) *The real part and* (b) *the imaginary part of the test image CiB.*

In general, when a bounded invariant set exists (as implied by Theorem 4.6) and no fixed point is attracting (e.g., with $\rho \geq 1$ in the inconsistent case), there tend to be some nontrivial attractors (limit cycles, strange attractors, ergodic invariant domain, etc.).

Nevertheless, the nonconvergent sequence controlled by the underlying attractors may still produce a reasonable solution under a proper termination rule. Our numerical experiments with noisy data confirm that this is indeed the case (see Figure 12). Analyzing the properties of such attractors is at the frontier of numerical analysis and beyond the scope of the present work.

7.1. Phase retrieval with noiseless data. We conduct a brief exploration of the optimal parameter for Gaussian-DRS. Our test image is 256-by-256 Cameraman+ i Barbara (CiB) (Figure 3). The resulting test object has the phase range $\pi/2$.

We use three baseline algorithms as benchmark. The first is AAR.

The second is Gaussian-DRS with $\rho = 1$

$$(7.2) \qquad \Gamma_1(u) = \frac{1}{2}u + \frac{1}{2}P_Y R_X u$$

(since $\mathcal{R}_Y$ in (3.11) is exactly P_Y with $\rho = 1$) given the basic guarantee that for $\rho \geq 0$ the regular solutions are attracting (Theorem 5.4), that for the range $\rho \geq 1$ no fixed points other than the regular solution(s) are locally attracting (Theorem 5.2), and that Gaussian-DRS with $\rho = 1$ produces the best convergence rate for any $\rho \geq 1$ (Corollary (6.2). The contrast between (7.2) and AAR (2.2) is noteworthy. The simplicity of the form (7.2) suggests the name *averaged projection reflection* (APR) algorithm.

The other, the relaxed AAR (RAAR), is one of the best performing phase retrieval algorithms defined by the map

$$(7.3) \qquad u_{k+1} = \beta\Gamma_0(u_k) + (1 - \beta)P_Y u_k, \quad \beta \in \left[\frac{1}{2}, 1\right],$$

where Γ_0 is the Gaussian-DRS map with $\rho = 0$ (i.e., AAR). RAAR becomes AAR for $\beta = 1$ (obviously) and AP for $\beta = \frac{1}{2}$ (after some calculation) [41, 36, 37].

After some rearrangement the fixed point equation for RAAR can be written as

$$P_X x + P_X^\perp x = \beta P_X^\perp x + (P_X + (1 - 2\beta)P_X^\perp)P_Y x,$$

from which it follows that

$$P_X x = P_X P_Y x, \quad P_X^\perp x = -\left(\frac{2\beta - 1}{1 - \beta}\right) P_X^\perp P_Y x$$

and hence

$$(7.4) \qquad P_X x - \left(\frac{1 - \beta}{2\beta - 1}\right) P_X^\perp x = P_X P_Y x + P_X^\perp P_Y x = P_Y x.$$

Notably this is exactly the same fixed point equation for Gaussian-DRS with the corresponding parameter

$$(7.5) \qquad \rho = \frac{1 - \beta}{2\beta - 1} \in [0, \infty)$$

which tends to 0 and ∞ as β tends to 1 and $\frac{1}{2}$, respectively. According to [34] the optimal β is usually between 0.8 and 0.9, corresponding to $\rho = 0.125$ and 0.333 according to (7.5). We set $\beta = 0.9$ in Figure 4.

In the experiments, we consider the setting of nonptychographic phase retrieval with two coded diffraction patterns; one is the plane wave ($\mu = 1$) and the other is $\mu = \exp(i\theta)$ where θ is independent and uniformly distributed over $[0, 2\pi)$. The theory of uniqueness of solution, up to a constant phase factor, is given in [16].

Figure 4 shows the relative error (RE; modulo a constant phase factor) versus iteration of RAAR ($\beta = 0.9$ round-bullet solid line), APR (blue-triangle dotted line), AAR (black-star dashed line), and Gaussian-DRS with (a) $\rho = 1.1$, (b) $\rho = 0.5$, (c) $\rho = 0.3$, and (d) $\rho = 0.1$. Note that the AAR, APR, and RAAR lines vary slightly across different plots because of random initialization.

The straight-line feature (in all but AAR) in the semi-log plot indicates global geometric convergence. The case with AAR is less clear in Figure 4. But it has been shown that the AAR sequence converges geometrically near the true object (after applying A^+) but converges in power-law ($\sim k^{-\alpha}$ with $\alpha \in [1, 2]$) from random initialization [9].

Figure 4 shows that APR outperforms AAR (consistent with the prediction of Corollary 6.4) but underperforms RAAR. By decreasing ρ to either 0.5 or 0.1, the performance of Gaussian-DRS closely matches that of RAAR. The optimal parameter appears to lie between 0.1 and 0.5. For example, with $\rho = 0.3$, Gaussian-DRS significantly outperforms RAAR. The oscillatory behavior of Gaussian-DRS in (d) is due to the dominant complex eigenvalue of J_A.

8. Blind ptychography algorithm. In the next two sections we apply the DRS methods to the more challenging problem of blind ptychography. In blind ptychography, we do not assume the full knowledge of the probe which is to be recovered simultaneously with the unknown object.
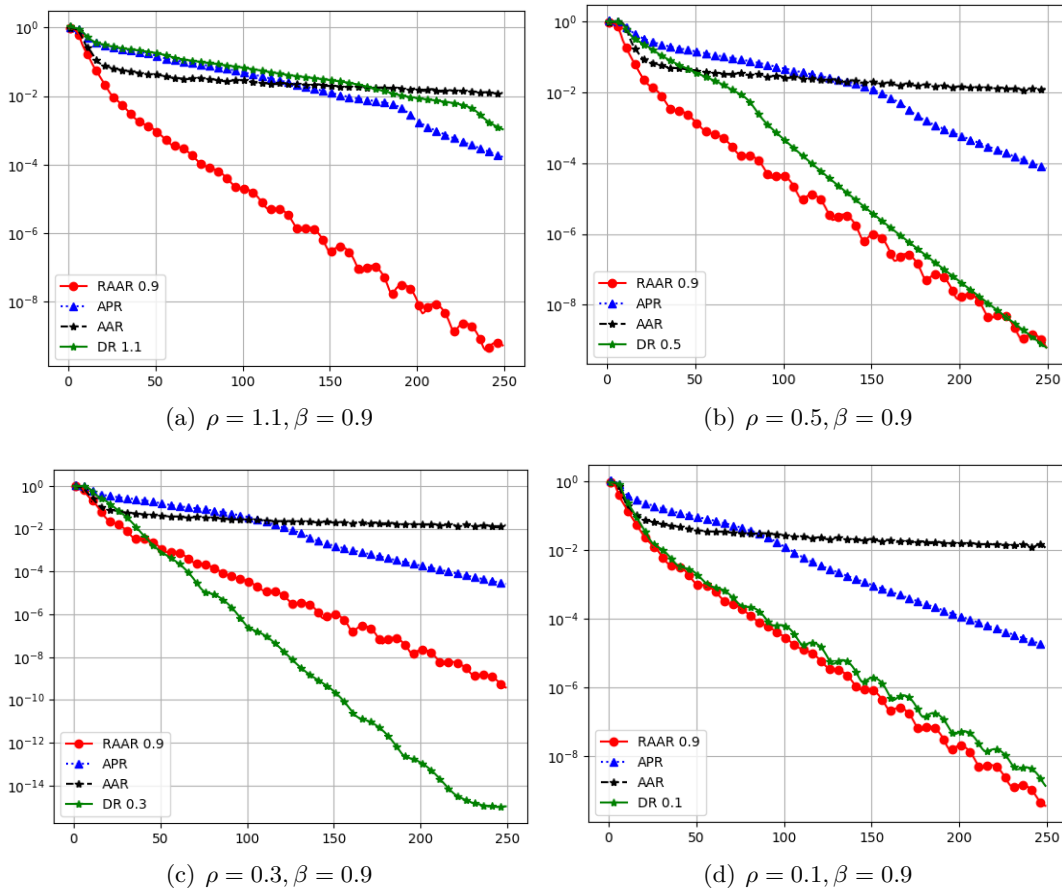
Figure 4. *Reconstruction (relative) error versus iteration by various methods indicated in the legend with random initialization. The straight-line feature (in all but AAR) in the semi-log plot indicates geometric convergence.*

Let ν^0 and $g = \vee_{\mathbf{t}} g^{\mathbf{t}}$ be any pair of the probe and the object estimates producing the same ptychography data as μ^0 and f, i.e., the diffraction pattern of $\nu^{\mathbf{t}} \odot g^{\mathbf{t}}$ is identical to that of $\mu^{\mathbf{t}} \odot f^{\mathbf{t}}$ where $\nu^{\mathbf{t}}$ is the $\mathbf{t}$-shift of ν^0 and $g^{\mathbf{t}}$ is the restriction of g to $\mathcal{M}^{\mathbf{t}}$. We refer to the pair (ν^0, g) as a blind-ptychographic solution (in the object domain) and (μ^0, f) as the true solution.

We can write the total measurement data as $b = |\mathcal{F}(\mu^0, f)|$ where $\mathcal{F}$ is the concatenated oversampled Fourier transform acting on $\{\mu^{\mathbf{t}} \odot f^{\mathbf{t}} : \mathbf{t} \in \mathcal{T}\}$ (see Appendix A), i.e., a bilinear transformation in the direct product of the probe space and the object space. By definition, a blind-ptychographic solution (ν^0, g) satisfies $|\mathcal{F}(\nu^0, g)| = b$.

There are two ambiguities inherent to any blind ptychography.

The first is the affine phase ambiguity. Consider the probe and object estimates

$$(8.1) \qquad \nu^0(\mathbf{n}) = \mu^0(\mathbf{n}) \exp(-\mathrm{i}a - \mathrm{i}\mathbf{w} \cdot \mathbf{n}), \quad \mathbf{n} \in \mathcal{M}^0,$$

$$(8.2) \qquad g(\mathbf{n}) = f(\mathbf{n}) \exp(\mathrm{i}b + \mathrm{i}\mathbf{w} \cdot \mathbf{n}), \quad \mathbf{n} \in \mathbb{Z}_n^2,$$

for any $a, b \in \mathbb{R}$ and $\mathbf{w} \in \mathbb{R}^2$. For any $\mathbf{t}$, we have the calculation

$$\begin{aligned}
\nu^{\mathbf{t}}(\mathbf{n}) &= \nu^0(\mathbf{n} - \mathbf{t}) \\
&= \mu^0(\mathbf{n} - \mathbf{t}) \exp(-i\mathbf{w} \cdot (\mathbf{n} - \mathbf{t})) \exp(-ia) \\
&= \mu^{\mathbf{t}}(\mathbf{n}) \exp(-i\mathbf{w} \cdot (\mathbf{n} - \mathbf{t})) \exp(-ia)
\end{aligned}$$

and hence $\forall \mathbf{n} \in \mathcal{M}^{\mathbf{t}}, \mathbf{t} \in \mathcal{T}$

$$(8.3) \qquad \nu^{\mathbf{t}}(\mathbf{n}) g^{\mathbf{t}}(\mathbf{n}) = \mu^{\mathbf{t}}(\mathbf{n}) f^{\mathbf{t}}(\mathbf{n}) \exp(i(b - a)) \exp(i\mathbf{w} \cdot \mathbf{t}).$$

Clearly, (8.3) implies that g and ν^0 produce the same ptychographic data as f and μ^0 since for each $\mathbf{t}$, $\nu^{\mathbf{t}} \odot g^{\mathbf{t}}$ is a constant phase factor times $\mu^{\mathbf{t}} \odot f^{\mathbf{t}}$ where $\odot$ is the entrywise (Hadamard) product. It is also clear that the above statement holds true regardless of the set $\mathcal{T}$ of shifts and the type of probe.

In addition to the affine phase ambiguity (8.1)–(8.2), a scaling factor ($g = cf, \nu^0 = c^{-1}\mu^0, c > 0$) is inherent to any blind ptychography. Note that when the probe is exactly known (i.e., $\nu^0 = \mu^0$), neither ambiguity can occur.

Besides the inherent ambiguities, blind ptychography imposes extra demands on the scanning scheme. For example, there are many other ambiguities inherent to the regular raster scan, $\mathcal{T} = \{\mathbf{t}_{kl} = \tau(k, l) : k, l \in \mathbb{Z}\}$, unless the step size $\tau = 1$. Blind ptychography with a raster scan produces τ-periodic ambiguities called the raster scan pathology as well as nonperiodic ambiguities associated with block phase drift. The reader to referred to [17] for a complete analysis of ambiguities associated with the raster scan.

A conceptually simple (though not necessarily the most practical) way to remove these ambiguities is introducing small irregular perturbations to the raster scan with $\tau > m/2$, i.e., the overlap ratio greater than 50% (see (9.5) and (9.6)). For a thorough analysis of the conditions for blind ptychography, we refer the reader to [18, 17].

The basic strategy for blind-ptychographic reconstruction is to alternately update the object and probe estimates starting from an initial guess as outlined in Algorithm 1 [51, 50, 19].

Algorithm 1. Alternating minimization.

1: Input: initial probe guess μ_1 and object guess f_1.
2: Update the object estimate $f_{k+1} = \arg \min L(A_k g)$ s.t. $g \in \mathbb{C}^{n \times n}$.
3: Update the probe estimate $\mu_{k+1} = \arg \min L(B_k \nu)$ s.t. $\nu \in \mathbb{C}^{m \times m}$.
4: Terminate if $\|\,|B_k \mu_{k+1}| - b\|$ stagnates or is less than tolerance; otherwise, go back to step 2 with $k \to k + 1$.

We solve the inner loops (steps 2 and 3 in Algorithm 1) and update the object and probe estimates by the DRS methods where $A_k h := \mathcal{F}(\mu_k, h), \forall h \in \mathbb{C}^{n^2}$, defines a matrix A_k for the kth probe estimate μ_k and $B_k \eta := \mathcal{F}(\eta, f_{k+1}), \forall \eta \in \mathbb{C}^{m^2}$, for the $(k + 1)$st image estimate f_{k+1}.

For ease of reference, we denote Algorithm 1 with Gaussian-DRS and Poisson-DRS by Gaussian-DRSAM and Poisson-DRSAM, respectively.

8.1. Initialization. For nonconvex iterative optimization, a good initial guess or some regularization is usually crucial for convergence [52, 6]. The initialization step is often glossed over in the development of numerical schemes. This is even more so for blind ptychography which is doubly nonconvex because, in addition to the phase retrieval step, extracting the probe and the object from their product is also nonconvex.

We say that a probe estimate ν^0 satisfies PPC(δ) (standing for the probe phase constraint) if

$$(8.4) \qquad \angle(\nu^0(\mathbf{n}), \mu^0(\mathbf{n})) < \delta\pi \quad \forall \mathbf{n},$$

where $\delta \in (0, 1/2]$ is the uncertainty parameter.

PPC(δ) defines an alternative measure to the standard norm-based metric. Our default case $\delta = 0.5$ with which PPC is equivalent to $\Re(\bar{\nu}^0 \odot \mu^0) > 0$ (where the bar denotes the complex conjugate) has the intuitive meaning that at every pixel ν^0 and μ^0 point to the same half plane in $\mathbb{C}$ (Figure 5).

Our initialization method is inspired by the uniqueness theory in [18] which proves PPC (0.5) is required to remove all ambiguities other than the inherent ones (the affine phase factor and the constant scaling factor).

Under PPC, however, the initial probe may be significantly far away from the true probe in norm. Even if $|\mu_1(\mathbf{n})| = |\mu^0(\mathbf{n})| = \text{const.}$, the probe guess with uniformly distributed ϕ in $(-\pi/2, \pi/2]$ has the RE close to

$$\sqrt{\frac{1}{\pi} \int_{-\pi/2}^{\pi/2} |e^{i\phi} - 1|^2 d\phi} = \sqrt{2\left(1 - \frac{2}{\pi}\right)} \approx 0.8525$$

with high probability. We use (8.4) for selecting and quantifying initialization, instead of the usual 2-norm. Nonblind ptychography gives rise to infinitesimally small δ. In practice, (8.4) needs only to hold for sufficiently large number of pixels $\mathbf{n}$.

In summary, in our numerical experiments we use the following probe initialization denoted by PPC:

$$(8.5) \qquad \mu_1(\mathbf{n}) = \mu^0(\mathbf{n}) \exp\left[i2\pi \frac{\mathbf{k} \cdot \mathbf{n}}{n}\right] \exp[i\phi(\mathbf{n})], \quad \mathbf{n} \in \mathcal{M}^0,$$

where $\phi(\mathbf{n})$ are independently and uniformly distributed on $(-\pi/2, \pi/2)$. In our numerical experiments, PPC results in geometric convergence for any $\mathbf{k}$ (even though the limiting solution may end up with a different $\mathbf{k}$ as allowed by linear phase ambiguity).
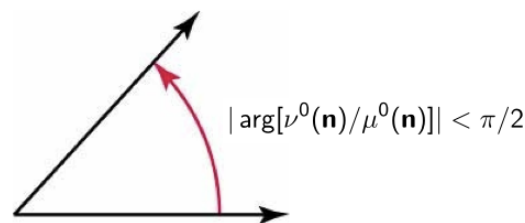

Figure 5. ν^0 *satisfies MPC if* $\nu_0(\mathbf{n})$ *and* $\mu^0(\mathbf{n})$ *form an acute angle* $\forall \mathbf{n}$.

9. Numerical experiments for blind ptychography. We test the DRS methods with $\rho = 1$ for blind ptychography and demonstrate that even with this far from optimal parameter (cf. Corollary 6.2 and Figure 4), DRSAM converges geometrically under the nearly minimum conditions established in the uniqueness theory [18] (see also sections 8.1 and 9.4).

The inner loops of Gaussian DRSAM become

$$u_k^{l+1} = \frac{1}{2}u_k^l + \frac{1}{2}b \odot \mathrm{sgn}\big(R_k u_k^l\big),$$

$$v_k^{l+1} = \frac{1}{2}v_k^l + \frac{1}{2}b \odot \mathrm{sgn}\big(S_k v_k^l\big),$$

and the inner loops of the Poisson DRSAM become

$$(9.1) \qquad u_k^{l+1} = \frac{1}{2}u_k^l - \frac{1}{3}R_k u_k^l + \frac{1}{6}\mathrm{sgn}\big(R_k u_k^l\big) \odot \sqrt{|R_k u_k^l|^2 + 24b^2},$$

$$(9.2) \qquad v_k^{l+1} = \frac{1}{2}v_k^l - \frac{1}{3}S_k v_k^l + \frac{1}{6}\mathrm{sgn}\big(S_k v_k^l\big) \odot \sqrt{|S_k v_k^l|^2 + 24b^2}.$$

Here $R_k = 2P_k - I$ is the reflector corresponding to the projector $P_k := A_k A_k^+$ and S_k is the reflector corresponding to the projector $Q_k := B_k B_k^+$. We set $u_k^1 = u_{k-1}^\infty$ where u_{k-1}^∞ is the terminal value at epoch $k - 1$ and $v_k^1 = v_{k-1}^\infty$ where v_{k-1}^∞ is the terminal value at epoch $k - 1$.

9.1. Test objects. In addition to CiB, our second test object is randomly phased phantom (RPP) defined by $f = P \odot e^{\mathrm{i}\phi}$ where P is the standard phantom (Figure 6(a)) and $\{\phi(\mathbf{n})\}$ are independent and identically distributed (i.i.d.) uniform random variables over $[0, 2\pi]$. RPP has the maximal phase range because of its noise-like phase profile. In addition to the huge phase range, RPP has loosely supported parts with respect to the measurement schemes (see below) due to its thick dark margins around the oval.
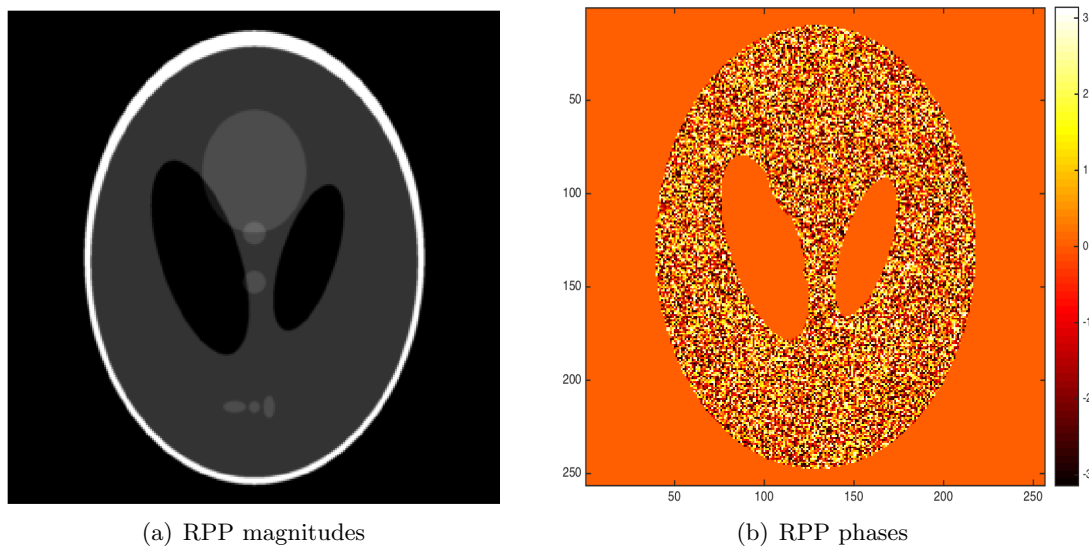

(a) RPP magnitudes   (b) RPP phases

Figure 6. (a) *Magnitudes and* (b) *phases of RPP.*

The third test object is the salted RPP, the sum of RPP and the salt noise (not shown). The salted noise is i.i.d. binomial random variables with probability 0.02 to be a complex constant in the form of $a(1+\mathrm{i}), a \in \mathbb{R}$, and probability 0.98 to be zero. The salt noise reduces the support looseness without significantly changing the original image making the salted RPP more connected with respect to the ptychographic measurement.

9.2. Probe function. We use a randomly phased probe with the unknown transmission function $\mu^0(\mathbf{n}) = e^{\mathrm{i}\theta(\mathbf{n})}$ where $\theta(\mathbf{n})$ are random variables. Randomly phased probes have been adopted in ptychographic experiments [42, 39, 46, 49].

We do not explore the issue of varying the probe size in the present work, which was carried out for AAR in [10]. We fix the probe size to 60×60. In addition to the i.i.d. probe, we consider a correlated probe produced by convolving the i.i.d. probe with characteristic function of the set $\{(k_1, k_2) \in \mathbb{Z}^2 : \max\{|k_1|, |k_2|\} \leq c \cdot m; \ c \in (0, 1]\}$ where the constant c is a measure of the correlation length in the unit of $m = 60$ (Figure 7).
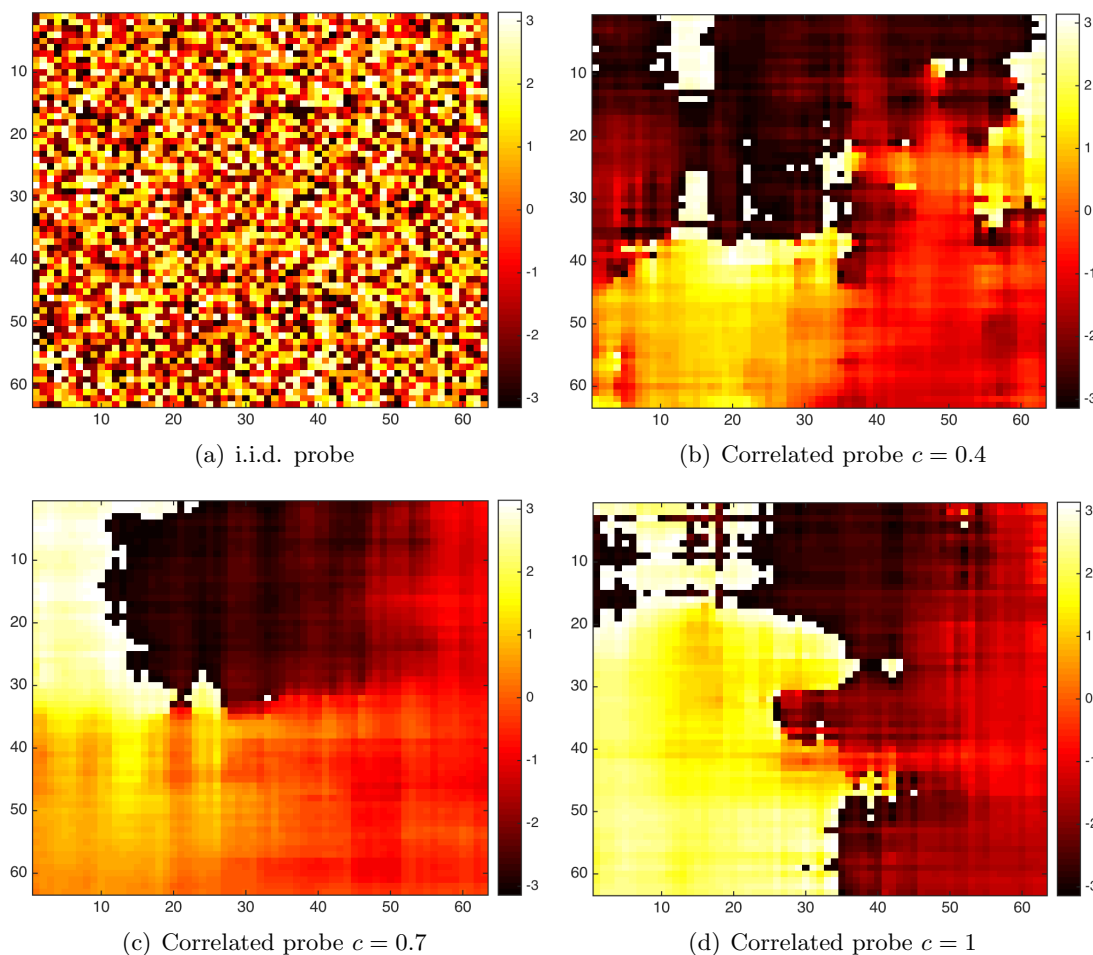

(a) i.i.d. probe

(b) Correlated probe $c = 0.4$

(c) Correlated probe $c = 0.7$

(d) Correlated probe $c = 1$

Figure 7. *The phase profile of* (a) *the i.i.d. probe and* (b), (c), (d) *the correlated probes of various correlation lengths.*

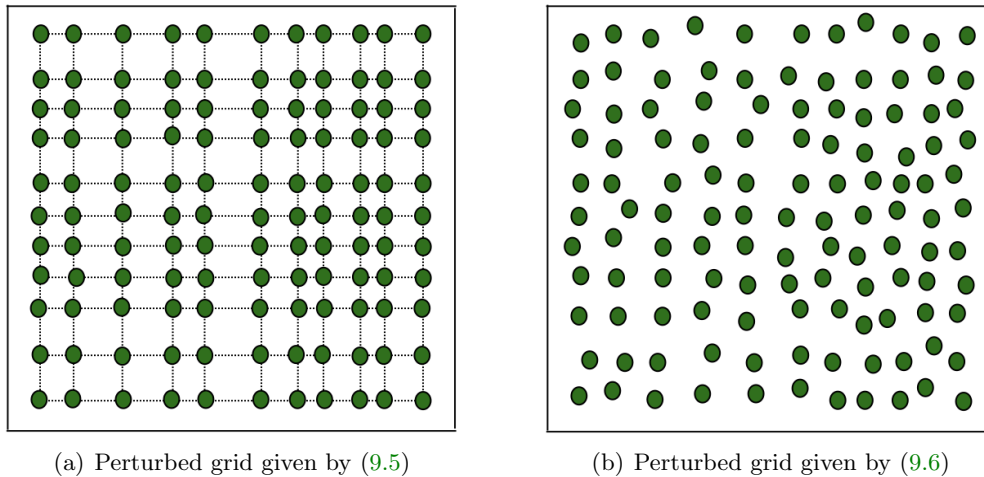(a) Perturbed grid given by (9.5)   (b) Perturbed grid given by (9.6)

Figure 8. *Two perturbed raster scans.*

9.3. Error metrics for blind ptychography. We use relative error (RE) and relative residual (RR) as the merit metrics for the recovered image f_k and probe μ_k at the kth epoch:

$$\text{(9.3)} \qquad \text{RE}(k) = \min_{\alpha \in \mathbb{C}, \mathbf{r} \in \mathbb{R}^2} \frac{\sqrt{\sum_{\mathbf{n}} |f(\mathbf{n}) - \alpha e^{-\mathrm{i}2\pi\mathbf{n}\cdot\mathbf{r}/n} f_k(\mathbf{n})|^2}}{\|f\|},$$

$$\text{(9.4)} \qquad \text{RR}(k) = \frac{\|b - |A_k f_k|\|}{\|b\|}.$$

Note that in (9.3) both the affine phase and the scaling factors are discounted.

9.4. Sampling schemes. The uniqueness theorem for blind ptychography [17] holds for the following irregularly perturbed raster scans:

$$\text{(9.5)} \qquad \text{Rank-one perturbation} \quad \mathbf{t}_{kl} = \tau(k,l) + (\delta_k^1, \delta_l^2), \quad k, l \in \mathbb{Z},$$

where δ_k^1 and δ_l^2 are small random variables relative to τ (Figure 8(a)). The other is

$$\text{(9.6)} \qquad \text{Full-rank perturbation} \quad \mathbf{t}_{kl} = \tau(k,l) + (\delta_{kl}^1, \delta_{kl}^2), \quad k, l \in \mathbb{Z},$$

where δ_{kl}^1 and δ_{kl}^2 are small random variables relative to τ (Figure 8(b)). Here the step size $\tau < m/2$ corresponding to the overlap ratio greater than 50%. The 50% overlap ratio has been proved to be a nearly minimum requirement for uniqueness with the perturbed raster scans.

We let δ_k^1 and δ_l^2 in the rank-one scheme (9.5) and δ_{kl}^1 and δ_{kl}^2 in the full-rank scheme (9.6) be i.i.d. uniform random variables over $[\![-4, 4]\!]$. In other words, the adjacent probes overlap by an average of $\tau/m = 50\%$.

9.5. Different combinations. First we compare performance of DRSAM with different combinations of loss functions, scanning schemes, and random probes in the case of noiseless
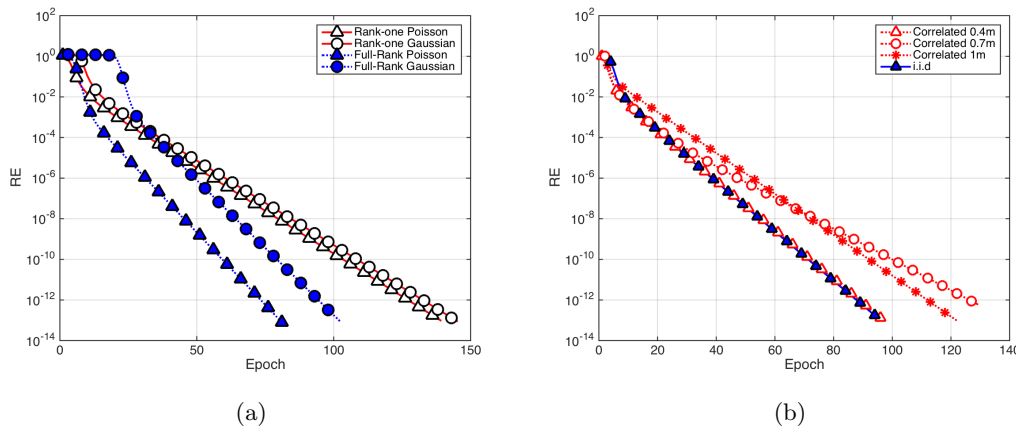
Figure 9. *Geometric convergence to CiB at various rates for* (a) *four combinations of loss functions and scanning schemes with i.i.d. probe (rank-one Poisson, rate = 0.8236; rank-one Gaussian, rate = 0.8258; full-rank Poisson, rate = 0.7205; full-rank Gaussian, rate = 0.7373) and* (b) *Poisson-DRS with four probes of different correlation lengths (rate = 0.7583 for c = 0.4; rate = 0.8394 for c = 0.7; rate = 0.7932 for c = 1; rate = 0.7562 for i.i.d. probe).*

measurements with the periodic boundary condition. We use the stopping criteria for the inner loops,

$$\frac{\||P_k u_k^l| - b\| - \||P_k u_k^{l+1}| - b\|}{\||P_k u_k^l| - b\|} \leq 10^{-4}$$

with the maximum number of iterations capped at 60.

Figure 9 shows geometric decay of RE (9.3) at various rates for the test object CiB. In particular, Figure 9(a) shows that the full-rank scheme outperforms the rank-one scheme and that Poisson-DRS outperforms (slightly) Gaussian-DRS, while Figure 9(b) shows that the i.i.d. probe yields the smallest rate of convergence (= 0.7562), closely followed by the rate (= 0.7583) for $c = 0.4$.

9.6. Boundary conditions. The periodic boundary condition conveniently treats all diffraction patterns and object pixels in the same way by assuming that $\mathbb{Z}_n^2$ is a (discrete) torus. The periodic boundary condition generally forces the slope **r** in the affine phase ambiguity to be integers. For three-dimensional blind tomography, however, different linear phase ramps from different projections would collectively create enormous three-dimensional ambiguities that are difficult to make consistent and hence it is highly desirable to remove the linear phase ambiguity early on in the process.

To this end, we consider the nonperiodic bright-field boundary conditions taking on some nonzero value in $\mathcal{M} \setminus \mathbb{Z}_n^2$. We aim to show that the affine phase ambiguity is absent under the bright-field boundary condition.

We test the Poisson-DRSAM with the full-rank scheme with a more stringent error metric

$$(9.7) \qquad\qquad \mathrm{RE2}(k) = \min_{\theta \in \mathbb{R}} \frac{\|f - e^{i\theta} f_k\|}{\|f\|}.$$

(a) Max iteration for inner loops = 80

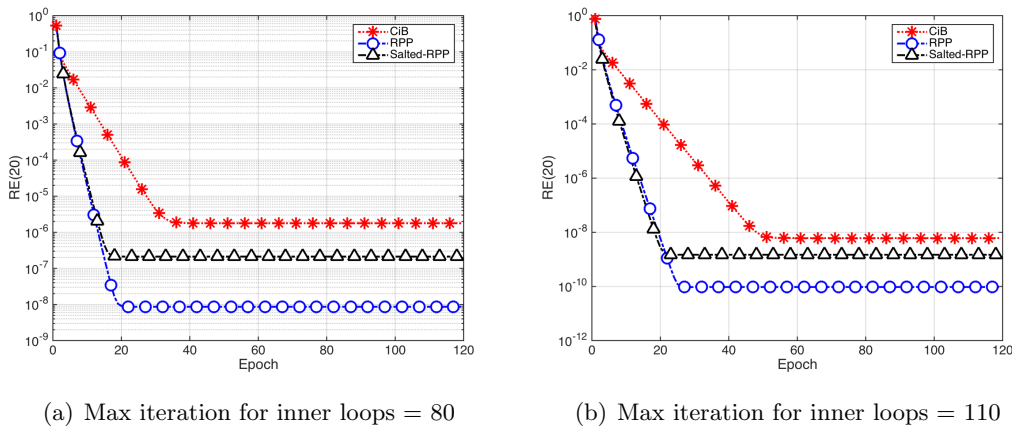(b) Max iteration for inner loops = 110

Figure 10. *RE2 under the bright-field condition = 255.*

We also use the less tolerant stopping rule

$$\frac{\|\,|P_k u_k^l| - b\| - \|\,|P_k u_k^{l+1}| - b\|}{\|\,|P_k u_k^l| - b\|} \leq 10^{-5}$$

for the inner loops with the maximum number of iteration capped at 80.

Figure 10 demonstrates the capability of the bright-field boundary condition (= 255) to eliminate the linear phase ambiguity as the stronger error metric (9.7) decays geometrically before settling down to the final level of accuracy. The final level of accuracy, however, depends on how accurately the inner loops for each epoch are solved. For example, increasing the maximum number of iteration from 80 (Figure 10(a)) to 110 (Figure 10(b)) significantly enhances the final accuracy of reconstruction.

We also see that the bright-field condition enforcement has a better result on RPP than CiB.

9.7. Comparison with rPIE. In this section, we compare the performance of DRSAM in Figure 10(a) with that of rPIE (regularized PIE) [38], the most up-to-date version of PIE.

Instead of using all 64 diffraction patterns simultaneously to update the object and probe estimates, rPIE uses one diffraction pattern at a time in a random order. As such rPIE is analogous to minibatch gradient descent in machine learning. The potential benefits include efficient memory use and a good speed boost by parallel computing resources. Unfortunately, rPIE often fails to converge in the current setting.

To obtain reasonable results for rPIE, we make two adjustments. First, we reduce the phase range of RPP from $(-\pi, \pi]$ to $(-\pi/2, \pi/2]$, which is an easier object to reconstruct. Second, for rPIE we use PPC(0.025) for the probe initialization, which restricts the probe phase uncertainty to $(-0.025\pi, 0.025\pi]$ instead of $(-\pi/2, \pi/2]$.

There are three adjustable parameters in rPIE and we select these values $\alpha = 0.95, \gamma_{\text{prb}} = 0.95, \gamma_{\text{obj}} = 0.9$ (see [38] for definitions). The order of updating small patches is randomly shuffled in each experiment. For each test image, we run 20 independent experiments and we
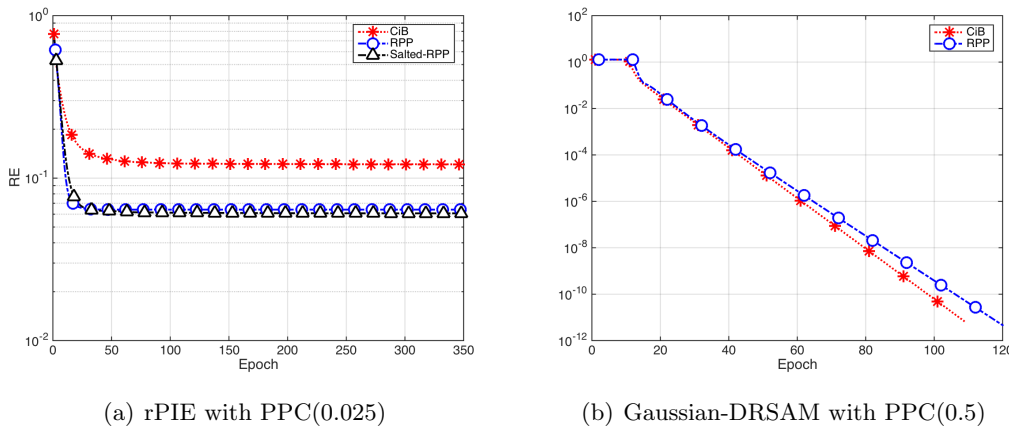
(a) rPIE with PPC(0.025)

(b) Gaussian-DRSAM with PPC(0.5)

Figure 11. *RE versus epoch for blind ptychography for various objects indicated in the legend by* (a) *rPIE and* (b) *DRSAM (RPP rate = 0.8015; CiB rate = 0.7787).*

present the best run in Figure 11. For ease of comparison, Figure 11(b) shows the corresponding results by Gaussian-DRSAM with $\rho = 1$.

9.8. Poisson noise. For noisy measurement, the level of noise is measured in terms of the noise-to-signal ratio (NSR),

$$\mathrm{NSR} = \frac{\||b - |Af|\||}{\|Af\|},$$

where A is the true measurement matrix and f the true object. Because the noise dimension N is roughly 16 times that of the object dimension, the feasibility problem is inconsistent with high probability.

Figure 12 shows RE versus NSR for CiB by Poisson-DRS and Gaussian-DRS with the periodic boundary condition, i.i.d. probe, and full-rank scheme. The maximum number of epochs in DRSAM is limited to 100. The RR stabilizes usually after 30 epochs. The (blue) reference straight line has slope = 1. We see that the Gaussian-DRS outperforms the Poisson-DRS, especially when the Poisson RE becomes unstable for NSR $\geq 35\%$. As noted in [38, 58, 11] fast convergence (with the Poisson log-likelihood function) may introduce noisy artifacts and reduce reconstruction quality.

Most important, Figure 12 confirms that though provably nonconvergent in the inconsistent case, Gaussian-DRSAM with $\rho = 1$ can yield reasonable solutions under practical termination rules.

10. Conclusion and discussion. We have presented and performed fixed point analysis for DRS methods of phase retrieval and ptychography based on the proximal relaxation of AAR with the relaxation parameter ρ.

For Gaussian-DRS, we have proved that for $\rho \geq 1$ all attracting fixed points must be regular solutions (Theorem 5.2) and that for $\rho \geq 0$ all regular solutions are attracting (Theorem 5.4). In other words, for $\rho \geq 1$, the problem of stagnation near a nonsolutional fixed point,
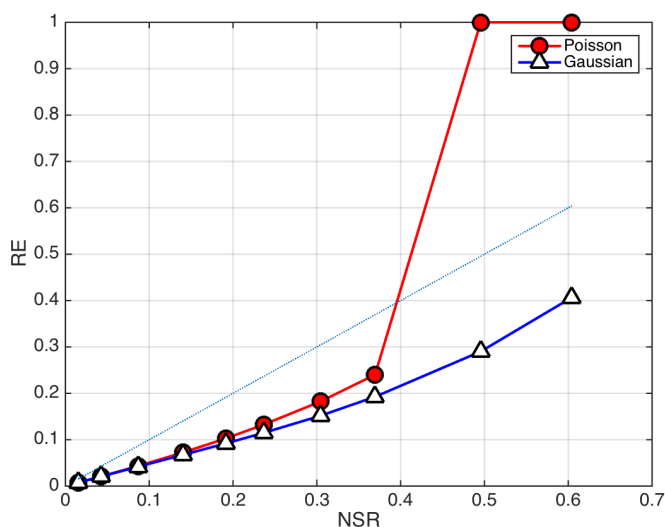
Figure 12. *RE versus NSR for reconstruction of CiB.*

a common problem with AP, is precluded. On the other hand, the problem of divergence (associated with AAR) in the inconsistent case does not arise in view of Theorem 4.6.

In addition, we have given an explicit formula for the optimal parameter ρ_* and the optimal rate of convergence in terms of the spectral gap (Corollary 6.2).

When applied to standard phase retrieval with two coded diffraction patterns, Gaussian-DRS converges geometrically from random initialization. When applied to blind ptychography, DRSAM, even with a far from optimal step size, converges geometrically under the nearly minimum conditions established in the uniqueness theory [18]. Our Python codes are posted on https://github.com/AnotherdayBeaux/Blind-Ptychography-GUI.

The holy grail of optimization approach has been finding a globally convergent algorithm whose underlying attractors are fixed points. It is worthwhile then to reflect on our results from the global convergence perspective of [33].

We have already pointed out that the analysis in [33] is not applicable to nondifferentiable loss functions. As discussed in section 7, this technical issue has a profound effect on the convergence behavior in the inconsistent case: Gaussian-DRS with $\rho \geq 1$ does not converge, globally or locally. This is an unexpected consequence of Theorem 5.2.

Our numerical experiments with noisy data, however, suggest that nonconvergent DRS sequences are nevertheless well-behaved (probably due to hitherto unknown well-controlled attractors) and produce a noise-amplification factor of about $\frac{1}{2}$ when terminated. Analysis of such (possibly strange) attractors and their impacts on numerics is an interesting topic for future research and at the frontier of numerical analysis.

Moreover, the global convergence framework is typically based on the construction of a nonincreasing merit function along the iterated sequence (i.e., Lyapunov-like function) that requires the step size (reciprocal of ρ) to be sufficiently small, resulting in slow convergence in practice.

Nice as it is, perhaps algorithmic convergence should not be our fixation in the case of noisy data. It may be more useful, for numerical purposes, to solve the noisy phase retrieval problem with algorithms with nontrivial (non-point-like) attractors which are necessarily nonconvergent in the traditional sense.

Appendix A. Measurement matrices. Let $\mathbb{Z}_n^2 = [\![0, n-1]\!]^2$ be the object domain containing the support of the discrete object f where $[\![k, l]\!]$ denotes the integers between, and including, $k \leq l \in \mathbb{Z}$. Let $\mathcal{M}^0 := \mathbb{Z}_m^2, m < n$, be the initial probe area, i.e., the support of the probe μ^0 describing the illumination field.

Let $\mathcal{T}$ be the set of all shifts, including $(0,0)$, involved in the ptychographic measurement. Denote by $\mu^{\mathbf{t}}$ the $\mathbf{t}$-shifted probe $\forall \mathbf{t} \in \mathcal{T}$ and $\mathcal{M}^{\mathbf{t}}$ the domain of $\mu^{\mathbf{t}}$. Let $f^{\mathbf{t}}$ be the object restricted to $\mathcal{M}^{\mathbf{t}}$. We refer to each $f^{\mathbf{t}}$ as a part of f and write $f = \vee_{\mathbf{t}} f^{\mathbf{t}}$ where $\vee$ is the "union" of functions consistent over their common support set. In ptychography, the original object is broken up into a set of overlapping object parts, each of which produces a $\mu^{\mathbf{t}}$-coded diffraction pattern. The totality of the coded diffraction patterns is called the ptychographic measurement data. For convenience, we assume the value zero for $\mu^{\mathbf{t}}, f^{\mathbf{t}}$ outside of $\mathcal{M}^{\mathbf{t}}$ and the periodic boundary condition on $\mathbb{Z}_n^2$ when $\mu^{\mathbf{t}}$ crosses over the boundary of $\mathbb{Z}_n^2$.

Let the μ-Fourier transform of f^0 be written as

$$F^0(\mathbf{w}) = \sum_{\mathbf{k} \in \mathcal{M}^0} e^{-\mathrm{i}2\pi \mathbf{k} \cdot \mathbf{w}} \mu^0(\mathbf{k}) f^0(\mathbf{k}), \quad \mathbf{w} = (w_1, w_2) \in [0, 1]^2,$$

and the μ-coded diffraction pattern as

$$(A.1) \qquad |F^0(\mathbf{w})|^2 = \sum_{\mathbf{k} \in \widetilde{\mathcal{M}}^0} \left\{ \sum_{\mathbf{k}' \in \mathcal{M}^0} \mu^0(\mathbf{k} + \mathbf{k}') f^0(\mathbf{k}' + \mathbf{k}) \overline{\mu^0(\mathbf{k}') f^0(\mathbf{k}')} \right\} e^{-\mathrm{i}2\pi \mathbf{k} \cdot \mathbf{w}},$$

where

$$\widetilde{\mathcal{M}}^0 = \{(k_1, k_2) \in \mathbb{Z}^2 : -m+1 \leq k_1 \leq m-1, -m+1 \leq k_2 \leq m-1\}.$$

Here and below the over-line notation means complex conjugacy. In view of (A.2), we sample the coded diffraction pattern on the grid

$$(A.2) \qquad L = \left\{ (w_1, w_2) \mid w_j = 0, \frac{1}{2m-1}, \frac{2}{2m-1}, \ldots, \frac{2m-2}{2m-1} \right\}.$$

We assume randomness in the phases θ of the mask function $\mu^0(\mathbf{n}) = |\mu^0|(\mathbf{n}) e^{\mathrm{i}\theta(\mathbf{n})}$ where $\theta(\mathbf{n})$ are independent, continuous real-valued random variables over $[0, 2\pi)$. We also require that $|\mu^0|(\mathbf{n}) \neq 0 \; \forall \mathbf{n} \in \mathcal{M}^0$.

Let $\mathcal{F}(\nu^0, g)$ be the bilinear transformation representing the totality of the Fourier (magnitude and phase) data for any probe ν and object g. From $\mathcal{F}(\nu^0, g)$ we can define two measurement matrices. First, for a given $\nu^0 \in \mathbb{C}^{m^2}$, let A_ν be defined via the relation $A_\nu g := \mathcal{F}(\nu^0, g) \; \forall g \in \mathbb{C}^{n^2}$; second, for a given $g \in \mathbb{C}^{n^2}$, let B_g be defined via $B_g \nu = \mathcal{F}(\nu^0, g) \; \forall \nu^0 \in \mathbb{C}^{m^2}$.
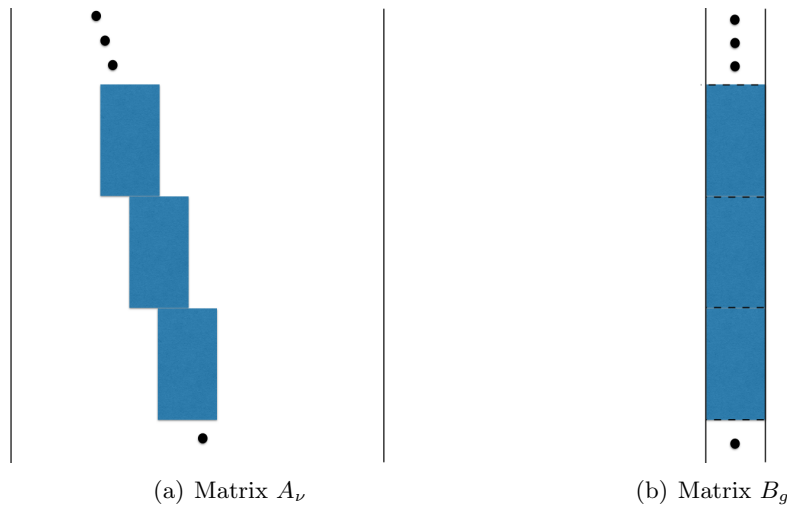
(a) Matrix A_ν (b) Matrix B_g

Figure 13. (a) A_ν *is a concatenation of shifted blocks* $\{\Phi\,\mathrm{diag}(\nu^{\mathbf{t}}) : \mathbf{t} \in \mathcal{T}\}$; *(b)* B_g *is a concatenation of unshifted blocks* $\{\Phi\,\mathrm{diag}(g^{\mathbf{t}}) : \mathbf{t} \in \mathcal{T}\}$. *In both cases, each block gives rise to a coded diffraction pattern* $|\Phi(\nu^{\mathbf{t}} \odot g^{\mathbf{t}})|$.

More specifically, let Φ denote the L-sampled Fourier matrix. The measurement matrix A_ν is a concatenation of $\{\Phi\,\mathrm{diag}(\nu^{\mathbf{t}}) : \mathbf{t} \in \mathcal{T}\}$ (Figure 13(a)). Likewise, B_g is $\{\Phi\,\mathrm{diag}(g^{\mathbf{t}}) : \mathbf{t} \in \mathcal{T}\}$ stacked on top of each other (Figure 13(b)). Since Φ has orthogonal columns, both A_ν and B_g have orthogonal columns and their pseudoinverses are efficient to compute.

We simplify the notation by setting $A = A_\mu$ and $B = B_f$.

Appendix B. The Poisson versus Gaussian log-likelihood functions. Consider the Poisson distribution

$$P(n) = \frac{\lambda^n e^{-\lambda}}{n!}.$$

Let $n = \lambda(1 + \epsilon)$ where $\lambda \gg 1$ and $\epsilon \ll 1$. Using Stirling's formula

$$n! \sim \sqrt{2\pi n}\, e^{-n} n^n$$

in the Poisson distribution, we obtain

$$P(n) \sim \frac{\lambda^{\lambda(1+\epsilon)} e^{-\lambda}}{\sqrt{2\pi}\, e^{-\lambda(1+\epsilon)}[\lambda(1+\epsilon)]^{\lambda(1+\epsilon)+1/2}}$$

$$\sim \frac{1}{\sqrt{2\pi\lambda}\, e^{-\lambda\epsilon}(1+\epsilon)^{\lambda(1+\epsilon)+1/2}}.$$

By the asymptotic

$$(1+\epsilon)^{\lambda(1+\epsilon)+1/2} \sim e^{\lambda\epsilon + \lambda\epsilon^2/2}$$

we have

(B.1) $$P(n) \sim \frac{e^{-\lambda\epsilon^2/2}}{\sqrt{2\pi\lambda}} = \frac{e^{-(n-\lambda)^2/(2\lambda)}}{\sqrt{2\pi\lambda}}.$$

Namely in the low noise limit the Poisson noise is equivalent to the Gaussian noise of the mean $|Af|^2$ and the variance equal to the intensity of the diffraction pattern. The overall NSR can be tuned by varying the signal energy $\|Af\|^2$.

The negative log-likelihood function for the right-hand side of (B.1) is

$$(\text{B.2}) \qquad \sum_j \ln |u[j]| + \frac{1}{2} \left| \frac{b[j]}{|u[j]|} - |u[j]| \right|^2, \quad b = \text{noisy diffraction pattern.}$$

For small NSR and in the vicinity of b, we make the substitution

$$\frac{\sqrt{b[j]}}{|u[j]|} \to 1, \quad \ln |u[j]| \to \ln \sqrt{b[j]}$$

to obtain

$$(\text{B.3}) \qquad \text{const.} + \frac{1}{2} \sum_j \left| \sqrt{b[j]} - |u[j]| \right|^2.$$

Appendix C. Equivalence between DRS and ADMM. We show that ADMM applied to the augmented Lagrangian

$$(\text{C.1}) \qquad \mathcal{L}(y, z) = K(y) + L(z) + \lambda^*(z - y) + \frac{\rho}{2}\|z - y\|^2$$

in the order alternatively as

$$(\text{C.2}) \qquad z_{k+1} = \arg\min_z \mathcal{L}(y_{k+1}, z, \lambda_k),$$

$$(\text{C.3}) \qquad y_{k+1} = \arg\min_x \mathcal{L}(y, z_k, \lambda_k),$$

$$(\text{C.4}) \qquad \lambda_{k+1} = \lambda_k + \rho(z_{k+1} - y_{k+1})$$

is equivalent to DRS.

Let

$$(\text{C.5}) \qquad z_{k+1} = \arg\min_z \mathcal{L}(y_k, z, \lambda_k) = \text{prox}_{L/\rho}(y_k - \lambda_k/\rho),$$

$$(\text{C.6}) \qquad y_{k+1} = \arg\min_x \mathcal{L}(y, z_{k+1}, \lambda_k) = \text{prox}_{K/\rho}(z_{k+1} + \lambda_k/\rho)$$

and consider the new variable

$$u_k := z_k + \lambda_{k-1}/\rho.$$

We have from (C.4) that

$$u_{k+1} = y_{k+1} + \lambda_{k+1}/\rho.$$

By (C.6), we also have

$$y_{k+1} = P_X(z_{k+1} + \lambda_k/\rho) = P_X u_{k+1}$$

and

$$y_k - \lambda_k/\rho = 2y_k - u_k = R_X u_k.$$

So (C.5) becomes

(C.7) $$z_{k+1} = \mathrm{prox}_{L/\rho}(R_X u_k).$$

Note also that by (C.4)

$$u_k - P_X u_k = \lambda_k/\rho$$

and hence

$$u_{k+1} = z_{k+1} + \lambda_k/\rho = u_k - P_X u_k + \mathrm{prox}_{L/\rho}(R_X u_k),$$

which is exactly the DRS scheme (3.14) after rearrangement.

Appendix D. Perturbation analysis of Poisson-DRS. The full analysis of the Poisson-DRS (3.15) is more challenging. Instead, we give a perturbative derivation of analogous result to Theorem 4.6 for the Poisson-DRS with small positive ρ.

For small ρ, by keeping only the terms up to $\mathcal{O}(\rho)$ we obtain the perturbed DRS:

(D.1) $$u_{k+1} = \frac{1}{2}u_k - \frac{1}{2}\left(1 - \frac{\rho}{2}\right) R_X u_k + P_Y R_X u_k.$$

Writing

$$I = P_X + P_X^\perp \quad \text{and} \quad R_X = P_X - P_X^\perp,$$

we then have the estimates

$$\|u_{k+1}\| \leq \|\frac{\rho}{4}P_X u_k + \left(1 - \frac{\rho}{4}\right) P_X^\perp u_k\| + \|P_Y R_X u_k\|$$
$$\leq \left(1 - \frac{\rho}{4}\right) \|u_k\| + \|b\|$$

since ρ is small. Iterating this bound, we obtain

$$\|u_{k+1}\| \leq \left(1 - \frac{\rho}{4}\right)^k \|u_1\| + \|b\| \sum_{j=0}^{k-1} \left(1 - \frac{\rho}{4}\right)^j$$

and hence

(D.2) $$\limsup_{k\to\infty} \|u_k\| \leq \frac{4}{\rho}\|b\|.$$

Note that the small ρ limit and the Poisson-to-Gaussian limit in Appendix B do not commune, resulting in a different constant in (D.2) from Theorem 4.6.

Appendix E. Eigenstructure. The vector space $\mathbb{C}^N = \mathbb{R}^N \oplus_{\mathbb{R}} i\mathbb{R}^N$ is isomorphic to $\mathbb{R}^{2N}$ via the map

$$V(v) := \begin{bmatrix} \Re(v) \\ \Im(v) \end{bmatrix} \quad \forall v \in \mathbb{C}^N$$

and endowed with the real inner product

$$\langle u, v \rangle := \Re(u^* v) = V(u)^\top V(v), \quad u, v \in \mathbb{C}^N.$$

We have

(E.1)
$$V(H\xi) = \begin{bmatrix} \Re[H]\Re[\xi] + \Im[H]\Im[\xi] \\ \Re[H]\Im[\xi] - \Im[H]\Re[\xi] \end{bmatrix} = \begin{bmatrix} \mathcal{H}^\top V(\xi) \\ \mathcal{H}^\top V(-i\xi) \end{bmatrix}, \quad \xi \in \mathbb{C}^n.$$

Let $\lambda_1 \geq \lambda_2 \geq \cdots \geq \lambda_{2n} \geq \lambda_{2n+1} = \cdots = \lambda_N = 0$ be the singular values of $\mathcal{H}$ in (5.16) with the corresponding right singular vectors $\{\eta_k \in \mathbb{R}^N\}_{k=1}^N$ and left singular vectors $\{\xi_k \in \mathbb{R}^{2n}\}_{k=1}^{2n}$. By definition, for $k = 1, \ldots, 2n$,

(E.2)
$$H^* \eta_k = \lambda_k G^{-1}(\xi_k),$$
(E.3)
$$\Re[HG^{-1}(\xi_k)] = \lambda_k \eta_k.$$

Proposition E.1. *We have* $\xi_1 = V(f), \xi_{2n^2} = V(-if), \lambda_1 = 1, \lambda_{2n^2} = 0$ *as well as* $\eta_1 = |Af|$.

Proof. Since

$$Hf = \Omega^* Af = |Af|$$

we have by (E.1)

(E.4)
$$\Re[Hf] = \mathcal{H}^\top \xi_1 = |Af|, \quad \Im[Hf] = \mathcal{H}^\top \xi_{2n^2} = 0$$

and hence the results. ∎

Corollary E.2.

(E.5)
$$\lambda_2 = \max\{\|\Im(Hu)\| : u \in \mathbb{C}^n, u \perp if, \|u\| = 1\}$$
$$= \max\{\|\mathcal{H}^\top u\| : u \in \mathbb{R}^{2n^2}, u \perp \xi_1, \|u\| = 1\}.$$

Proof. By (E.1),

$$\Im[Hu] = \mathcal{H}^\top V(-iu).$$

The orthogonality condition $iu \perp f$ is equivalent to

$$V(x_0) \perp V(-iu).$$

Hence, by Proposition E.1 ξ_2 is the maximizer of the right-hand side of (E.5), yielding the desired value λ_2. ∎

Proposition E.3. *For $k = 1, \ldots, 2n^2$,*

$$\lambda_k^2 + \lambda_{2n^2+1-k}^2 = 1, \tag{E.6}$$

$$\xi_{2n^2+1-k} = V(-\mathrm{i}V^{-1}(\xi_k)), \tag{E.7}$$

$$\xi_k = V(\mathrm{i}V^{-1}(\xi_{2n^2+1-k})). \tag{E.8}$$

Proof. Since H is an isometry, we have $\|w\| = \|Hw\| \ \forall w \in \mathbb{C}^n$. On the other hand, we have

$$\|Hw\|^2 = \|V(Hw)\|^2 = \|\mathcal{H}^\top V(w)\|^2 + \|\mathcal{H}^\top V(-\mathrm{i}w)\|^2$$

and hence

$$\|V(w)\|^2 = \|\mathcal{H}^\top V(w)\|^2 + \|\mathcal{H}^\top V(-\mathrm{i}w)\|^2. \tag{E.9}$$

Now we prove (E.6), (E.7), and (E.8) by induction.

Recall the variational characterization of the singular values/vectors

$$\lambda_j = \max \|\mathcal{H}^\top u\|, \xi_j = \arg\max \|\mathcal{H}^\top u\|, \text{s.t. } u \perp \xi_1, \ldots, \xi_{j-1}, \quad \|u\| = 1. \tag{E.10}$$

By Proposition E.1, (E.6), (E.7), and (E.8) hold for $k = 1$. Suppose (E.6), (E.7), and (E.8) hold for $k = 1, \ldots, j-1$ and we now show that they also hold for $k = j$.

Hence by (E.9)

$$\lambda_j^2 = \max_{\|u\|=1} \|\mathcal{H}^\top u\|^2 = 1 - \min_{\|v\|=1} \|\mathcal{H}^\top v\|^2, \quad \text{s.t. } u \perp \xi_1, \ldots, \xi_{j-1}, \quad v = V(-\mathrm{i}V^{-1}(u)).$$

The condition $u \perp \xi_1, \ldots, \xi_{j-1}$ implies $v \perp \xi_{2n^2}, \ldots, \xi_{2n^2+2-j}$ and vice versa. By the dual variational characterization to (E.10)

$$\lambda_{2n^2+1-j} = \min \|\mathcal{H}^\top u\|, \xi_{2n^2+1-j} = \arg\min \|\mathcal{H}^\top u\|, \text{s.t. } u \perp \xi_{2n^2}, \ldots, \xi_{2n^2+2-j}, \|u\| = 1,$$

we have

$$\lambda_j^2 = 1 - \lambda_{2n^2+1-j}^2, \quad \xi_{2n^2+1-j} = V(-\mathrm{i}V^{-1}(\xi_j)). \qquad \blacksquare$$

Proposition E.4. *For each $k = 1, \ldots, 2n^2$,*

$$HH^*\eta_k = \lambda_k(\lambda_k\eta_k + \mathrm{i}\lambda_{2n^2+1-k}\eta_{2n^2+1-k}), \tag{E.11}$$

$$HH^*\eta_{2n^2+1-k} = \lambda_{2n^2+1-k}(\lambda_{2n^2+1-k}\eta_{2n^2+1-k} - \mathrm{i}\lambda_k\eta_k) \tag{E.12}$$

implying

$$HH^* = \begin{bmatrix} \lambda_k^2 & \lambda_k\lambda_{2n^2+1-k} \\ \lambda_k\lambda_{2n^2+1-k} & \lambda_{2n^2+1-k}^2 \end{bmatrix}$$

in the basis of $\eta_k, \mathrm{i}\eta_{2n^2+1-k}$.

Proof. By definition, $\mathcal{H}\eta_k = \lambda_k \xi_k$. Hence

$$H^*\eta_k = (\Re[H^*] + \mathrm{i}\Im[H^*])\eta_k = \lambda_k(\xi_k^{\mathrm{R}} + \mathrm{i}\xi_k^{\mathrm{I}}),$$

where

$$\xi_k = \begin{bmatrix} \xi_k^{\mathrm{R}} \\ \xi_k^{\mathrm{I}} \end{bmatrix}, \quad \xi_k^{\mathrm{R}}, \xi_k^{\mathrm{I}} \in \mathbb{R}^n.$$

On the other hand, $\mathcal{H}^\top \xi_k = \lambda_k \eta_k$ and hence

$$\text{(E.13)} \qquad \Re[H]\xi_k^{\mathrm{R}} - \Im[H]\xi_k^{\mathrm{I}} = \lambda_k \eta_k.$$

Now we compute $HH^*\eta_k$ as follows:

$$\text{(E.14)} \qquad \begin{aligned} HH^*\eta_k &= \lambda_k H(\xi_k^{\mathrm{R}} + \mathrm{i}\xi_k^{\mathrm{I}}) \\ &= \lambda_k(\Re[H] + \mathrm{i}\Im[H])(\xi_k^{\mathrm{R}} + \mathrm{i}\xi_k^{\mathrm{I}}) \\ &= \lambda_k(\Re[H]\xi_k^{\mathrm{R}} - \Im[H]\xi_k^{\mathrm{I}}) + \mathrm{i}\lambda_k(\Re[H]\xi_k^{\mathrm{I}} + \Im[H]\xi_k^{\mathrm{R}}) \\ &= \lambda_k^2 \eta_k + \mathrm{i}\lambda_k(\Re[H]\xi_k^{\mathrm{I}} + \Im[H]\xi_k^{\mathrm{R}}) \end{aligned}$$

by (E.13)

Notice that

$$\text{(E.15)} \qquad \begin{aligned} \Re(H)\xi_k^{\mathrm{I}} + \Im(H)\xi_k^{\mathrm{R}} &= \mathcal{H}^\top \begin{bmatrix} \Re(-\mathrm{i}V^{-1}(\xi_k)) \\ \Im(-\mathrm{i}V^{-1}(\xi_k)) \end{bmatrix} \\ &= \mathcal{H}^\top V(-\mathrm{i}V^{-1}(\xi_k)) \\ &= \mathcal{H}^\top \xi_{2n^2+1-k} \\ &= \lambda_{2n^2+1-k}\eta_{2n^2+1-k} \end{aligned}$$

by Proposition E.3.

Putting (E.14) and (E.15) together, we have (E.11). Likewise, (E.12) follows from a similar calculation. ∎

REFERENCES

[1] H. H. BAUSCHKE AND J. M. BORWEIN, *On projection algorithms for solving convex feasibility problems*, SIAM Rev., 38 (1996), pp. 367–426.

[2] H. H. BAUSCHKEA, J. Y. B. CRUZ, T. T. A. NGHIA, H. M. PHAN, AND X. WANG, *The rate of linear convergence of the Douglas-Rachford algorithm for subspaces is the cosine of the Friedrichs angle*, J. Approx. Theory, 185 (2014), pp. 63–79.

[3] H. H. BAUSCHKE, P. L. COMBETTES, AND D. R. LUKE, *Phase retrieval, error reduction algorithm, and Fienup variants: a view from convex optimization*, J. Opt. Soc. Am. A, 19 (2002), pp. 13341–13345.

[4] H. H. BAUSCHKE, P. L. COMBETTES, AND D. R. LUKE, *Hybrid projection-reflection method for phase retrieval*, J. Opt. Soc. Am. A, 20 (2003), pp. 1025–1034.

[5] H. H. Bauschke, P. L. Combettes, and D. R. Luke, *Finding best approximation pairs relative to two closed convex sets in Hilbert space*, J. Approx. Theory, 127 (2004), pp. 178–192.

[6] L. Bian, J. Suo, J. Chung, X. Ou, C. Yang, F. Chen, and Q. Dai, *Fourier ptychographic reconstruction using Poisson maximum likelihood and truncated Wirtinger gradient*, Sci. Rep., 6 (2016), 27384.

[7] O. Bunk, M. Dierolf, S. Kynde, I. Johnson, O. Marti, and F. Pfeiffer, *Influence of the overlap parameter on the convergence of the ptychographical iterative engine*, Ultramicroscopy, 108 (2008), pp. 481–487.

[8] H. Chang, P. Enfedaque, and S. Marchesini, *Blind ptychographic phase retrieval via convergent alternating direction method of multipliers*, SIAM J. Imaging Sci., 12 (2019), pp. 153–185.

[9] P. Chen and A. Fannjiang, *Phase retrieval with a single mask by Douglas-Rachford algorithms*, Appl. Comput. Harmon. Anal., 44 (2018), pp. 665–699.

[10] P. Chen and A. Fannjiang, *Coded-aperture ptychography: uniqueness and reconstruction*, Inverse Problems, 34 (2018), 025003.

[11] P. Chen, A. Fannjiang, and G. Liu, *Phase retrieval with one or two coded diffraction patterns by alternating projection with the null initialization*, J. Fourier Anal. Appl., 24 (2018), pp. 719–758.

[12] M. Dierolf, A. Menzel, P. Thibault, P. Schneider, C. M. Kewish, R. Wepf, O. Bunk, and F. Pfeiffer, *Ptychographic x-ray computed tomography at the nanoscale*, Nature, 467 (2010), pp. 436–439.

[13] J. Douglas and H. H. Rachford, *On the numerical solution of heat conduction problems in two and three space variables*, Trans. Amer. Math. Soc., 82 (1956), pp. 421–439.

[14] J. Eckstein and D. P. Bertsekas, *On the Douglas-Rachford splitting method and the proximal point algorithm for maximal monotone operators*, Math. Program. A, 55 (1992), pp. 293–318.

[15] V. Elser, *Phase retrieval by iterated projections*, J. Opt. Soc. Am. A, 20 (2003), pp. 40–55.

[16] A. Fannjiang, *Absolute uniqueness of phase retrieval with random illumination*, Inverse Problems, 28 (2012), 075008.

[17] A. Fannjiang, *Raster grid pathology and the cure*, Multiscale Model. Simul., 17 (2019), pp. 973–995.

[18] A. Fannjiang and P. Chen, *Blind ptychography: Uniqueness and ambiguities*, Inverse Problems, 36 (2020), 045005.

[19] A. Fannjiang and W. Liao, *Fourier phasing with phase-uncertain mask*, Inverse Problems, 29 (2013), 125001.

[20] A. Fannjiang and Z. Zhang, *Blind Ptychography by Douglas-Rachford Splitting*, https://arxiv.org/abs/1809.00962, 2018.

[21] H. M. L. Faulkner and J. M. Rodenburg, *Movable aperture lensless transmission microscopy: A novel phase retrieval algorithm*, Phys. Rev. Lett., 93 (2004), 023903.

[22] H. M. L. Faulkner and J. M. Rodenburg, *Error tolerance of an iterative phase retrieval algorithm for moveable illumination microscopy*, Ultramicroscopy, 103 (2005), pp. 153–164.

[23] J. R. Fienup, *Phase retrieval algorithms: A comparison*, Appl. Opt., 21 (1982), pp. 2758–2769.

[24] J. R. Fienup and C. C. Wackerman, *Phase-retrieval stagnation problems and solutions*, J. Opt. Soc. Am. A, 3 (1986), pp. 1897–1907.

[25] D. Gabay and B. Mercier, *A dual algorithm for the solution of nonlinear variational problems via finite element approximation*, Comput. Math. Appl., 2 (1976), pp. 17–40.

[26] P. Giselsson and S. Boyd, *Linear convergence and metric selection for Douglas-Rachford splitting and ADMM*, IEEE Trans. Automat. Control, 62:2 (2017), pp. 532–544.

[27] R. Glowinski and A. Marroco, *Sur l'approximation, par éléments finis d'ordre un, et la résolution, par pénalisation-dualité d'une classe de problémes de dirichlet non linéaires*, ESAIM Math. Model. Numer. Anal., 9 (1975), pp. 41–76.

[28] P. Godard, M. Allain, V. Chamard, and J. Rodenburg, *Noise models for low counting rate coherent diffraction imaging*, Opt. Express, 20 (2012), pp. 25914–25934.

[29] B. He and X. Yuan, *On the $\mathcal{O}(1/m)$ convergence rate of the Douglas-Rachford alternating direction method*, SIAM J. Numer. Anal., 50 (2012), pp. 700–709.

[30] R. Hesse, D. R. Luke, S. Sabach, and M. K. Tam, *Proximal heterogeneous block implicit-explicit method and application to blind ptychographic diffraction imaging*, SIAM J. Imaging Sci., 8 (2015), pp. 426–457.

[31] A. P. KONIJNENBERG, W. M. J. COENE, AND H. P. URBACH, *Model-independent noise-robust extension of ptychography*, Opt. Exp., 26 (2018), pp. 5857–5874.

[32] C. KUANG, Y. MA, R. ZHOU, J. LEE, G. BARBASTATHIS, R. R. DASARI, Z. YAQOOB, AND P. T. C. SO, *Digital micromirror device-based laser-illumination Fourier ptychographic microscopy*, Opt. Exp., 23 (2015), pp. 26999–27010.

[33] G. LI AND T. K. PONG, *Douglas-Rachford splitting for nonconvex optimization with application to nonconvex feasibility problems*, Math. Program. A 159 (2016), pp. 371–401.

[34] J. LI AND T. ZHOU, *On relaxed averaged alternating reflections (RAAR) algorithm for phase retrieval with structured illumination*, Inverse Problems, 33 (2017), 025012.

[35] P.-L. LIONS AND B. MERCIER, *Splitting algorithms for the sum of two nonlinear operators*, SIAM J. Numer. Anal., 16 (1979), pp. 964–979.

[36] D. LUKE, *Relaxed averaged alternating reflections for diffraction imaging*, Inverse Problems, 21 (2005), pp. 37–50.

[37] D. LUKE, *Finding best approximation pairs relative to a convex and prox-regular set in a Hilbert space*, SIAM J. Optim., 19 (2008), pp. 714–739.

[38] A. M. MAIDEN, D. JOHNSON, AND P. LI, *Further improvements to the ptychographical iterative engine*, Optica, 4 (2017), pp. 736–745.

[39] A. M. MAIDEN, G. R. MORRISON, B. KAULICH, A. GIANONCELLI, AND J. M. RODENBURG, *Soft X-ray spectromicroscopy using ptychography with randomly phased illumination*, Nat. Commun., 4 (2013), 1669.

[40] A. M. MAIDEN AND J. M. RODENBURG, *An improved ptychographical phase retrieval algorithm for diffractive imaging*, Ultramicroscopy, 109 (2009), pp. 1256–1262.

[41] S. MARCHESINI, H. KRISHNAN, B. J. DAURER, D. A. SHAPIRO, T. PERCIANO, J. A. SETHIAN, AND F. R. MAIA, *SHARP: a distributed GPU-based ptychographic solver*, J. Appl. Crystallogr., 49 (2016), pp. 1245–1252.

[42] G. R. MORRISON, F. ZHANG, A. GIANONCELLI, AND I. K. ROBINSON, *X-ray ptychography using randomized zone plates*, Opt. Exp., 26 (2018), pp. 14915–14927.

[43] Y. S. G. NASHED, D. J. VINE, T. PETERKA, J. DENG, R. ROSS, AND C. JACOBSEN, *Parallel ptychographic reconstruction*, Opt. Exp., 22 (2014), pp. 32082–32097.

[44] K. A. NUGENT, *Coherent methods in the X-ray sciences*, Adv. Phys., 59 (2010), pp. 1–99.

[45] X. OU, G. ZHENG, AND C. YANG, *Embedded pupil function recovery for Fourier ptychographic microscopy*, Opt. Exp., 22 (2014), pp. 4960–4972.

[46] X. PENG, G. J. RUANE, M. B. QUADRELLI, AND G. A. SWARTZLANDER, *Randomized apertures: High resolution imaging in far field*, Opt. Express, 25 (2017), 296187.

[47] F. PFEIFFER, *X-ray ptychography*, Nat. Photon., 12 (2017), pp. 9–17.

[48] J. M. RODENBURG AND H. M. L. FAULKNER, *A phase retrieval algorithm for shifting illumination*, Appl. Phys. Lett., 85 (2004), 4795.

[49] M. STOCKMAR, P. CLOETENS, I. ZANETTE, B. ENDERS, M. DIEROLF, F. PFEIFFER, AND P. THIBAULT, *Near-field ptychography: Phase retrieval for inline holography using a structured illumination*, Sci. Rep., 3 (2013), 1927.

[50] P. THIBAULT, M. DIEROLF, O. BUNK, A. MENZEL, AND F. PFEIFFER, *Probe retrieval in ptychographic coherent diffractive imaging*, Ultramicroscopy, 109 (2009), pp. 338–343.

[51] P. THIBAULT, M. DIEROLF, A. MENZEL, O. BUNK, C. DAVID, AND F. PFEIFFER, *High-resolution scanning X-ray diffraction microscopy*, Science, 321 (2008), pp. 379–382.

[52] P. THIBAULT AND M. GUIZAR-SICAIROS, *Maximum-likelihood refinement for coherent diffractive imaging*, New J. Phys., 14 (2012), 063004.

[53] L. TIAN, Z. LIU, L.-H. YEH, M. CHEN, J. ZHONG, AND L. WALLER, *Computational illumination for high-speed in vitro Fourier ptychographic microscopy*, Optica, 2 (2015), pp. 904–911.

[54] Z. WEN, C. YANG, X. LIU, AND S. MARCHESINI, *Alternating direction methods for classical and ptychographic phase retrieval*, Inverse Problems, 28 (2012), 115010.

[55] L. YEH, J. DONG, J. ZHONG, L. TIAN, M. CHEN, G. TANG, M. SOLTANOLKOTABI, AND L. WALLER, *Experimental robustness of Fourier ptychography phase retrieval algorithms*, Opt. Exp., 23 (2015), pp. 33214–33240.

[56] Y. ZHANG, P. SONG, AND Q. DAI, *Fourier ptychographic microscopy using a generalized Anscombe transform approximation of the mixed Poisson-Gaussian likelihood*, Opt. Exp., 25 (2017), pp. 168–179.

[57] G. ZHENG, R. HORSTMEYER, AND C. YANG, *Wide-field, high-resolution Fourier ptychographic microscopy*, Nat. Photonics, 7 (2013), pp. 739–745.

[58] C. ZUO, J. SUN, AND Q. CHEN, *Adaptive step-size strategy for noise-robust Fourier ptychographic microscopy*, Opt. Exp., 24 (2016), pp. 20724–20744.